

Recent Advances in Memristive Materials for Artificial Synapses

Sun Gil Kim, Ji Su Han, Hyojung Kim, Soo Young Kim, and Ho Won Jang**

Neuromorphic architectures are in the spotlight as promising candidates for substituting current computing systems owing to their high operation speed, scale-down ability, and, especially, low energy consumption. Among candidate materials, memristors have shown excellent synaptic behaviors such as spike time-dependent plasticity and spike rate-dependent plasticity by gradually changing their resistance state according to electrical input stimuli. Memristor can work as a single synapse without programming support, which remarkably satisfies the requirements of neuromorphic computing. Here, the most recent developments in memristor-based artificial synapses are introduced with their excellent synaptic behaviors accompanied with detailed explanation of their working mechanisms. As conventional memristive materials, metal oxides are reviewed with recent advancements in heterojunction technologies. An overview of organic materials is presented with their remarkable synaptic behaviors including their advantages of biocompatibility, low cost, complementary metal-oxide semiconductor compatibility, and ductility. 2D materials are also introduced as promising candidates for artificial synapses owing to their flexibility and scalability. As emerging materials, halide perovskites and low-dimensional materials are presented with their synaptic behaviors. In the last section, future challenges and research directions are discussed. This review article is hoped to be a guide to rational materials design for the artificial synapses of neuromorphic computing.

1. Introduction

Because of data explosion in the smart world, requirements for memories are becoming complicated and meet the limitations under the current technologies. In order to store and operate lots of data, memories which provide high operation speeds, low energy consumption, and scale-down ability have been strongly

required. Several types of emerging memories have been researched in the past few decades such as magnetic memory, phase change memory, ferroelectric tunnel junctions, and resistive switching memory. Among these emerging devices, resistive switching memory called memristors, introduced by Chua in 1971,^[1] have strong points of small cell size, nonvolatile and random data access possibility, easy fabrication process, and simple structure.^[2,3] Because of these advantages, various materials are examined for achieving memristive properties.

In addition, different from the past several decades, information is being made depending on experiences or repeated stimuli similar to that in the human brain. The human brain contains $\approx 10^{11}$ neurons and 10^{15} synapses, occupies a small space, and consumes less than 20 W, which is lower than the power required to run a household light bulb.^[4–6] Moreover, the human brain is currently considered as the most intelligent and fastest operation system. Therefore, neuromorphic computing, which emulates the human brain, has been regarded as a promising next-generation computing

system. Studies on neuromorphic computing have been rapidly growing and highlighted for various applications such as artificial intelligence, sensors, robotic devices, and memory devices.

Existing neural networks are implemented by the combination of machine learning as software and the von Neumann architecture as hardware based on the complementary metal-oxide semiconductor (CMOS) technology. However, CMOS-based circuits require 6–12 transistors and the design is not flexible.^[7] The present computing system with the von Neumann architecture is implemented by a serial operation through a central processing unit (CPU). Because of the von Neumann bottleneck, memory devices have limitations in data processing speed between memory and CPU and require high power and large space.^[8–10] Therefore, a new neuromorphic computing system that is executed by parallel operation with a high operation speed, low energy consumption, and small volume is critically required.

To achieve such requirement, memristive materials have been actively examined as emulating several functions of human brain. A memristor could act as a single unit of synapse without software programming supports. Memristor-based neuromorphic architecture is implemented by parallel operation with efficient power, small volume, and high data processing

S. G. Kim, J. S. Han, H. Kim, Prof. H. W. Jang
Department of Materials Science and Engineering
Research Institute of Advanced Materials
Seoul National University
Seoul 08826, Republic of Korea
E-mail: hwjang@snu.ac.kr

Prof. S. Y. Kim
School of Chemical Engineering and Materials Science
Chung-Ang University
Seoul 06974, Republic of Korea
E-mail: sooyoungkim@cau.ac.kr

 The ORCID identification number(s) for the author(s) of this article can be found under <https://doi.org/10.1002/admt.201800457>.

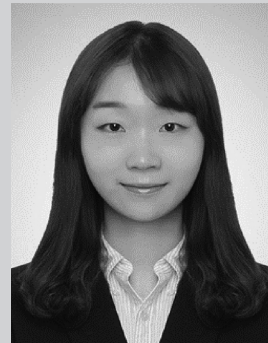
DOI: 10.1002/admt.201800457

speed. There are various possible materials that can achieve memristive properties. These include binary oxides,^[11–21] oxide perovskites,^[22–25] polymers,^[26–30] bioinspired materials,^[31–36] 2D materials,^[37–44] halide perovskites,^[5,45,46] and low-dimensional materials^[47–51] as shown in **Figure 1**. Each material has advantages in the working mechanism and/or properties of itself, which results in improved performances of memristive devices and artificial synapses.

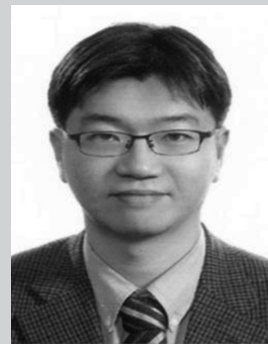
Memristive devices consist of metal/insulator/metal structures. The two metals act as the top electrode and the bottom electrode. Generally, voltages are induced to the top electrode while the bottom electrode is grounded. By applying direct current (DC) voltages or programmed pulse voltages on the top electrode, the insulator material resistance states changes to a low resistance state (LRS) or high resistance state (HRS) depending on the polarity of the voltage, material characteristics, and device structure. If the resistance state of the insulator material is changed from HRS to LRS, it is called a SET operation and considered as a “write” process. On the other hand, if the resistance state is converted from LRS to HRS, it is called a RESET operation, and means an “erase” process.^[52,53] The resistance change is caused by filamentary^[54,55] or interface type switching.^[56,57] For digital type memories, the SET and RESET mean the data “1” and “0,” respectively. However, for analog type memories, especially artificial synapses, gradual resistance changes are required to reflect consecutive electrical stimuli. Therefore, the resistive switching mechanism should be controlled according to the requirements of devices.

Studies for achieving synaptic functions with memristors and fabricating neuromorphic device systems are actively conducted in the past few years. Furthermore, there are several review papers about the research progress on neuromorphic applications. The review paper published by Kuzum et al. in 2013^[6] summarized the progress of synaptic electronics including phase change, resistive change, and ferroelectric change devices before 2013. It also introduced field-effect transistor (FET)-based synaptic devices and compared the performances of each type of device. In 2017, Wang et al.^[4] analyzed the strategies of recent developments in synaptic functions, conducting filament (CF) control mechanisms, and the correlation among materials. More recently, Hadiyawarman et al. in 2018^[58] introduced neuromorphic devices based on carbon, silicon, and other materials. There are also review articles focusing on resistive layer materials. In 2016, Qu et al.^[59] summarized the recent progress in neuromorphic applications of WO_x -based memristors including thickness and doping effects. In addition, Gao et al.^[60] in 2016 reported a review article about metal oxide memristor-based synaptic devices including device designs.

Besides these efforts on studying the neuromorphic architecture with various materials, devices, and resistive switching mechanisms, there are still requirements for demonstrating the characteristics of memristors and their improved synaptic functions depending on each type of material. This paper focuses on insulator materials of memristors that can achieve not only a resistive switching when working as a nonvolatile memory but also synaptic characteristics when acting as an artificial synapse, which is a basic building block for neuromorphic computing. Here, requirements for artificial synapses are demonstrated according to the biological synaptic functions

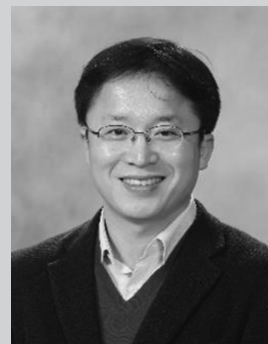


Sun Gil Kim received her B.S. degree at the department of Materials Science and Engineering from Sungkyunkwan University in 2012. After which she joined Samsung Electronics since 2012. She is an M.S. candidate at the department of Materials Science and Engineering in Seoul National University. Her research interests focus on organic-inorganic and all-inorganic halide perovskites and their applications of memristors and artificial synapses.



Soo Young Kim is a Professor of the Department of Chemical Engineering and Materials Science in Chung-Ang University. He received the Ph.D. degree in materials science and engineering from Pohang University of Science and Technology, Pohang, South Korea in 2007. After his postdoctoral period in

Georgia Institute of Technology, USA, he joined Chung-Ang University in 2009. He is interested in the modulation of the properties of 2D materials such as graphene, graphene oxide, transition metal dichalcogenides, and halide perovskites, and their applications. He combined his experience about optoelectronic devices with 2D materials and halide perovskites so that his research is focused on the optimization of 2D materials' properties and their application to energy devices, such as OLEDs, organic photovoltaics, perovskite solar cells, light emitting diodes, and gas sensors.



Ho Won Jang is an Associate Professor of the Department of Materials Science and Engineering in Seoul National University. He earned his Ph.D. from the Department of Materials Science and Engineering in Pohang University of Science and Technology in 2004. He worked as a Research Associate at University of Wisconsin-

Madison from 2006 to 2009. Before he joined Seoul National University in 2012, he worked in Korea Institute of Science and Technology as a Senior Research Scientist. His research interests include the synthesis of oxides, 2D materials, and halide perovskites and their applications for nanoelectronics, solar water splitting cells, chemical sensors, plasmonics, metal-insulator transition, and ferroelectricity.

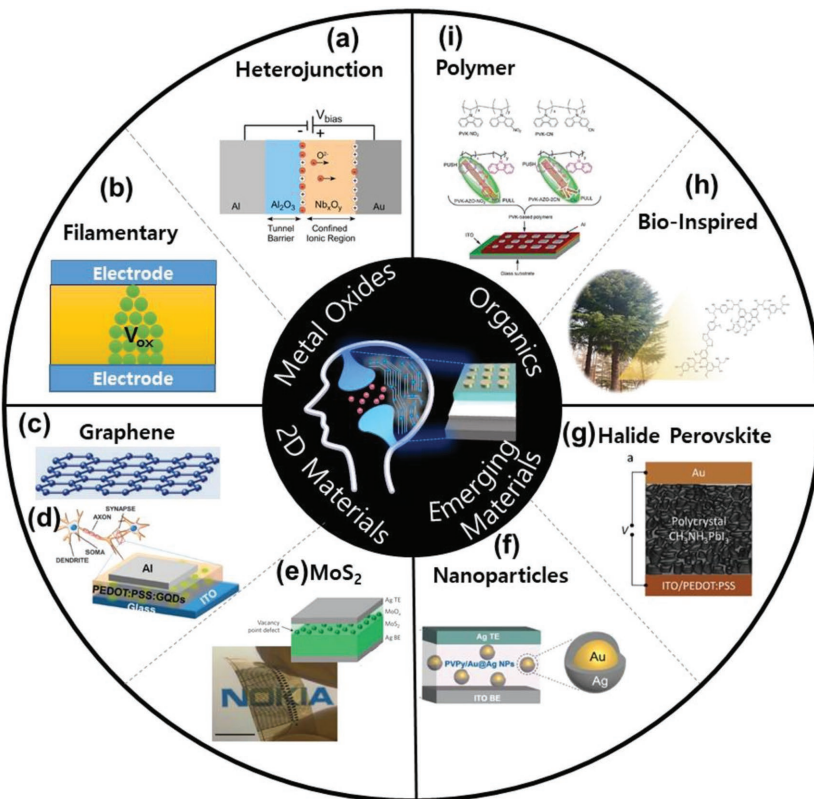


Figure 1. Recent memristive materials applied for artificial synapses: metal oxides, organic materials, 2D materials, and emerging materials. a) Schematic of heterojunction structure of Al/Al₂O₃/Nb_xO_y/Au device. Reproduced under the terms of the CC-BY Creative Commons Attribution 4.0 International License.^[91] Copyright 2015, Springer Nature. b) Schematic of filamentary switching in metal oxides memristors. c) 2D flat shape of graphene. Reproduced with permission.^[106] Copyright 2014, Springer Nature. d) Schematic of graphene quantum dot based artificial synapse. Reproduced under the terms of the CC-BY Creative Commons Attribution 4.0 International License.^[114] Copyright 2017, Springer Nature. e) Two-terminal MoS₂-based memristors and a photograph of transparent MoO_x/MoS₂ film. Reproduced with permission.^[43] Copyright 2014, Springer Nature. f) A two terminal memristor with a structure of PVPy@Au@Ag nanoparticles sandwiched between a Ag top electrode and an indium tin oxide (ITO) bottom electrode. Reproduced with permission.^[48] Copyright 2018, Wiley-VCH. g) Schematics of a Au/CH₃NH₃PbI₃/PEDOT:PSS/ITO artificial synapse. Reproduced with permission.^[45] Copyright 2016, Wiley-VCH. h) A chemical structure of lignin extracted from plants. Reproduced with permission.^[31] Copyright 2017, American Chemical Society. i) Chemical structures and a schematic diagram of Al/PVK-based polymer/ITO device. Reproduced with permission.^[125] Copyright 2011, Wiley-VCH.

(Section 2). Then, resistive switching mechanisms are introduced with their shapes and formation processes depending on the device materials (Section 2). In the succeeding sections, recent developments of each material that achieves synaptic behaviors are reviewed by categorizing the types of dielectric materials as metal oxides, organic materials, 2D materials, halide perovskites, and emerging materials.

2. Requirements for Artificial Synapses

2.1. Comparison between Biological Synapses and Artificial Synapses

Neurons are nerve cells that compose the human brain and they are connected to each other by synapses as shown in

Figure 2a. When a neuron receives an electrical signal, it transfers the signal to the postneuron by generating an electrical spike called action potential through the synapses. The action potential contains signals by which the brain acquires, analyzes, and conveys information.^[52] As shown in Figure 2b, when a neuron receives the action potential, transmitters are synthesized and stored in vesicles. The depolarization of the presynaptic terminal opens the Ca²⁺ channel, and then the vesicles are emitted to the synaptic cleft. These contact points of 20–40 nm gaps between preneuron and postneuron are called synapses. Passing through the synaptic cleft, they bind to the receptor molecules of Na⁺ channel in the postsynaptic membrane.^[6,61] In this process, the spike from the preneuron can be transmitted to the postneuron.

An artificial synapse consists of a top electrode, which emulates the preneuron, a bottom electrode as the postneuron, and an insulator, which acts as the synapse, as illustrated in Figure 2c. The conductivity and resistance of the devices represent the strength of connection between the preneuron and postneuron.^[5] Researchers are interested not only on the insulator materials but also on the top and bottom electrodes, because the interaction between the three materials affects the device performance. Usually the bottom electrodes are inert metals or oxides that induce ground voltage, whereas the top electrodes are active electrodes made of inert or active metals. However, insulator materials are more vigorously studied, from oxides to halide perovskites, and the structures of materials also vary from 3D to 1D. Hence, this article introduces the artificial synapses with classification of insulator materials.

2.2. Spike Timing-Dependent Plasticity

Each neuron has 10³ to 10⁴ synapses through which the neuron is connected to other neurons. Synapses modulate the connection strength according to neural activities called synaptic plasticity.^[6] Hence, it is important to concentrate on the parameters that affect synaptic plasticity. One of the parameters is called spike time-dependent plasticity (STDP). In 1949, Hebbian^[62–64] suggested the basis for learning and memory modeling by mentioning that if an axon is enough to excite another axon and participates in firing it continuously, growth processes or metabolic changes occur in one or both cells. In other words, Hebbian stated that the synaptic strength between a preneuron and postneuron varies if both of them are simultaneously active and this is possibly the “first law” of synaptic plasticity. As shown in Figure 3a, a conventional Hebbian learning rule indicated

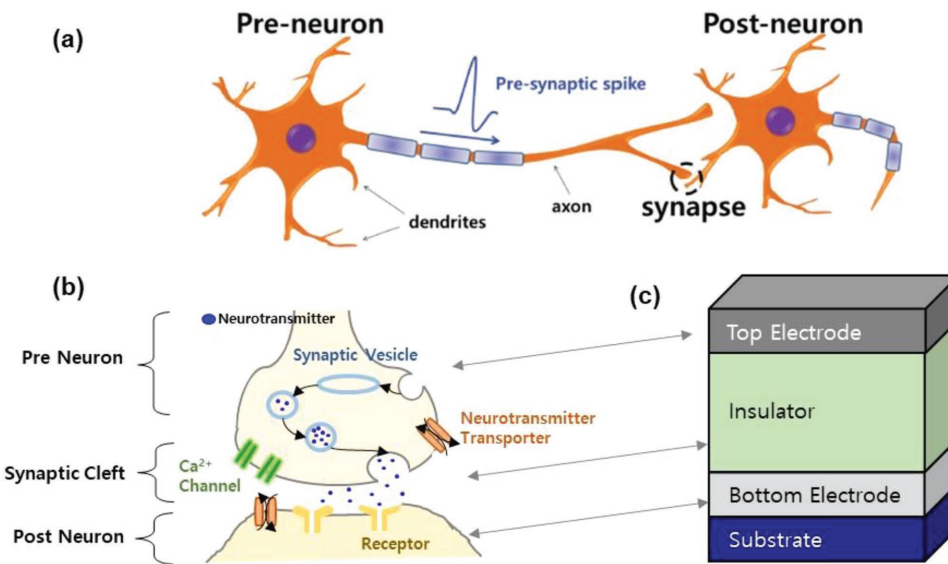


Figure 2. Comparison between biological synapses and artificial synapses. a) Schematic diagram of a preneuron, postneuron, and synapse. Reproduced with permission.^[5] Copyright 2016, Wiley-VCH. b) Schematic diagram of neurotransmission process. c) A general structure of two terminal memristors-based artificial synapses.

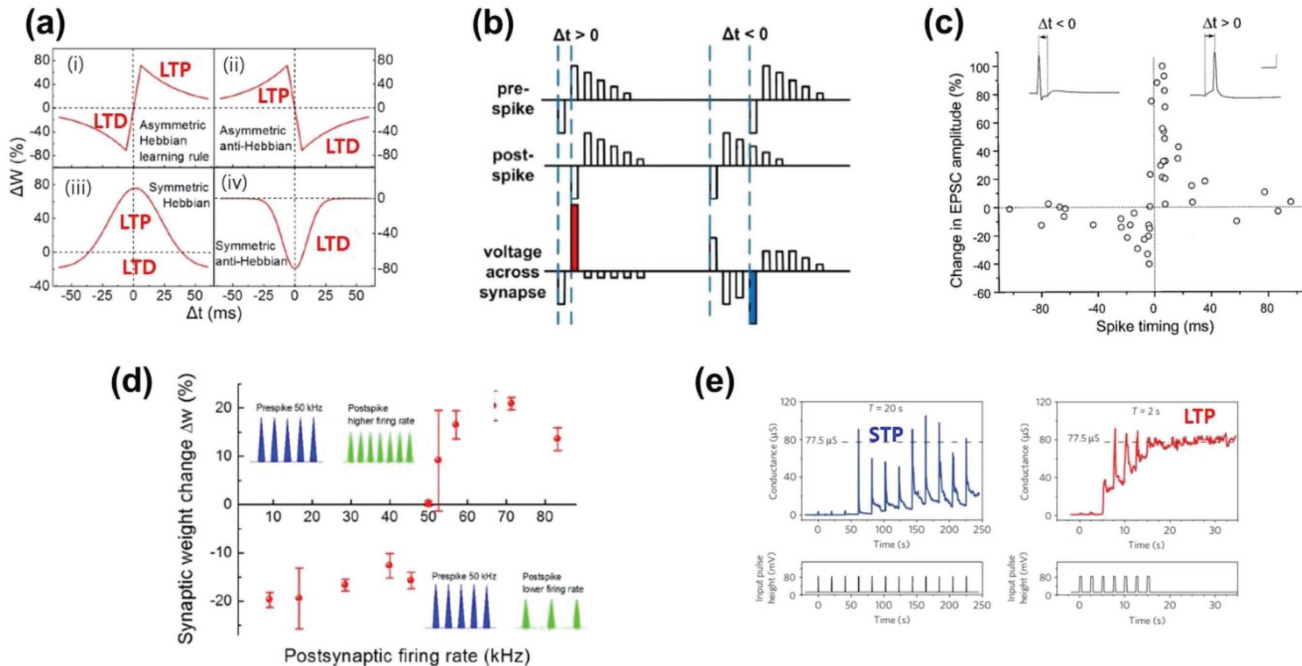


Figure 3. Two representative synaptic behaviors; STDP and SRDP. a) Asymmetric, symmetric Hebbian learning rule and asymmetric, symmetric anti-Hebbian learning rule which explain synaptic weight change according to the pre- and postspike time difference, Δt . Reproduced with permission.^[65] Copyright 2014, Springer Nature. b) STDP realization schemes with programmed prespike and postspike voltage in an artificial synapse. Reproduced with permission.^[94] Copyright 2011, IEEE. c) A STDP behavior of a biological synapse which follows asymmetric Hebbian learning rule. Reproduced with permission.^[66] Copyright 1998, Society for Neuroscience. d) SRDP data achieved by an inorganic memristor. It suggests the dependence of postsynaptic firing rate. If it is higher than prespike (50 kHz), the synapse is potentiated. On the other hand, if it is lower than 50 kHz, the synapse is depressed. Reproduced with permission.^[65] Copyright 2014, Springer Nature. e) Relation of input pulse interval on the conductance of artificial synapse. When the input pulse height is the same, the synapse is short term potentiated by large interval of input pulse while it is long term potentiated by narrow interval of input pulse. Reproduced with permission.^[67] Copyright 2011, Springer Nature.

that the synaptic weight Δw is a function of time Δt . If a prespike comes before a postspike, Δt is positive and the polarity of Δw is positive; however, if a prespike follows a postspike, Δt is negative and the polarity of Δw is either positive or negative. The Hebbian learning rule is categorized into four different cases as shown in Figure 3a: asymmetric, symmetric Hebbian, and anti-Hebbian learning rules. In the case of Figure 3a(i),(ii), the synaptic weight is decided by the order of timing between prespikes and postspikes. However, in other cases, only the relative timing difference between two spikes affects Δw as described in Figure 3a(iii),(iv). In all cases, as the absolute value of Δt decreases, the absolute value of Δw rises. It means that the prespike is generated slightly before the postspike, and spontaneously the postspike is created. If Δt is positive, the spike is potentiated and Δt is smaller while the synaptic strength becomes stronger. By contrast, if Δt has a negative polarity, the spike signal is depressed and Δt is smaller while the synaptic strength becomes weaker (Figure 3b). Li et al.^[65] fitted the STDP as a time function by

$$\Delta w = \begin{cases} A_+ e^{-|\Delta t|/\tau_+} & \text{if } \Delta t > 0 \\ A_- e^{-|\Delta t|/\tau_-} & \text{if } \Delta t < 0 \end{cases} \quad (1)$$

where A_{\pm} and τ_{\pm} represent the scaling factor and the time constant of the function respectively. In 1998, Bi and Poo.^[66] successfully displayed the percentage change in excitatory postsynaptic current (EPSC) of a biological synapse at 20–30 min after a continuous correlated spiking (60 pulses at 1 Hz) as shown in Figure 3c. It appears similar to the asymmetric Hebbian learning rule shown in Figure 3a(i).

2.3. Spike Rate-Dependent Plasticity

The second learning rule is called spike rate-dependent plasticity (SRDP). As shown in Figure 3d, Li et al.^[65] investigated the rate-dependent learning with a AgInSbTe electronic synapse by inducing triangle voltage pulses with 5 μ s increasing time and 5 μ s declining time. The voltage amplitudes of prespikes are 1.2 V and those of postspikes are 0.8 V. The presynaptic average firing rate is fixed at 50 kHz, and the postsynaptic average firing rate is changed from 10 to 83 kHz. If the postspike firing rate is higher at 50 to 83 kHz, the percentage of synaptic weight change Δw is positive. By contrast, if the postspike firing rate is lower at 10 to 50 kHz, Δw has a negative polarity. As mentioned in the previous section, the polarity of Δw represents potentiation and depression. If the postspike rate exceeds that of the prespike, the synaptic strength becomes stronger, but if it is lower than that of the prespike, the synaptic strength is depressed. Additionally, SRDP could be explained by the repetition time of input pulse. As shown in Figure 3e, Ohno et al.^[67] plotted the conductance versus the interval of input pulses with Ag₂S inorganic synapses. They applied input pulses with an amplitude (V) of 80 mV, a width of 0.5 s, and repeated intervals of 2 or 20 s. When the repeated pulse interval is 20 s, the conductance decays to its initial low value after each pulse. This means that memristor-based synapses could change the conductance without any applied voltage by

sensitively reacting to the applied pulses. Because it rapidly declines to its initial value after the pulse, this state is called short-term potentiation (STP). On the other hand, when the repeated pulse interval is 2 s, the conductance is maintained at higher values even though pulses are not applied anymore. It is clearly observed that the repeated application of shorter interval pulses continuously increases the conductance state without any decrease. In this case, the synapses are in a long-term potentiation (LTP) state.

2.4. Potentiation and Depression

In biology, potentiation and depression are parameters of the synaptic weight; a positive value represents potentiation, and a negative value indicates depression. Both STDP by the Hebbian learning rule and SRDP determine the polarity of synaptic weight according to the spike timing and spike firing rate. Potentiation and depression are divided into four values: STP, LTP, short-term depression (STD), and long-term depression (LTD).^[45,68,69] STP is determined through the temporal rise of the synaptic weight, which is followed by a rapid decline to its original state. However, repeated input pulses generate a permanent change, which is called LTP state. In the case of a negative value of synaptic weight, the temporal decay of synaptic strength indicates an STD state, but a permanent low value of synaptic weight represents an LTD state.^[61,67] This activity-dependent modification facilitates the information process and storage in the human brain.

In 1968, Atkinson and Shiffrin^[70] denoted the structural features of the human memory system as described in Figure 4c. The first process of memory is immediate registration of sensory stimulus. The second process is the short-term storage, which is expected to disappear or be removed completely after several times. The last major process is the long-term storage, which does not decay or become lost permanently. The short-term memory could be related to STP and the long-term memory to LTP. In memristor-based artificial synapses, the short-term and long-term memories can be emulated by the type of CF. In 2011, Ohno et al.^[67] drew schematics of the formation of Ag filament by input pulses in a Ag₂S synapse. If the input pulses are not enough to generate a Ag atom bridge, the synapse acts as STP. However, if the input pulses are enough to form a Ag filament bridge, the synapse works as LTP (Figure 4a). In addition, in 2016, Berdan et al.^[71] plotted the energy versus conductance observed in synaptic connections (Figure 4b). The STP state occurs in volatile type by metastable phase transition. From STP, a long-term phase change for a nonvolatile switching called LTP could be encouraged by the formation of a stable conducting bridge. The stable transition to a high energy state with a low conductance is also possibly formed.

2.5. Advanced Synaptic Plasticity

Recently, researchers have demonstrated advanced concepts of synaptic plasticity such as metaplasticity and heteroplasticity in order to achieve more delicate imitation of human brain. In 2016, Tan et al.^[21] demonstrated the metaplasticity which stores the previous changes of synaptic plasticity and shows different

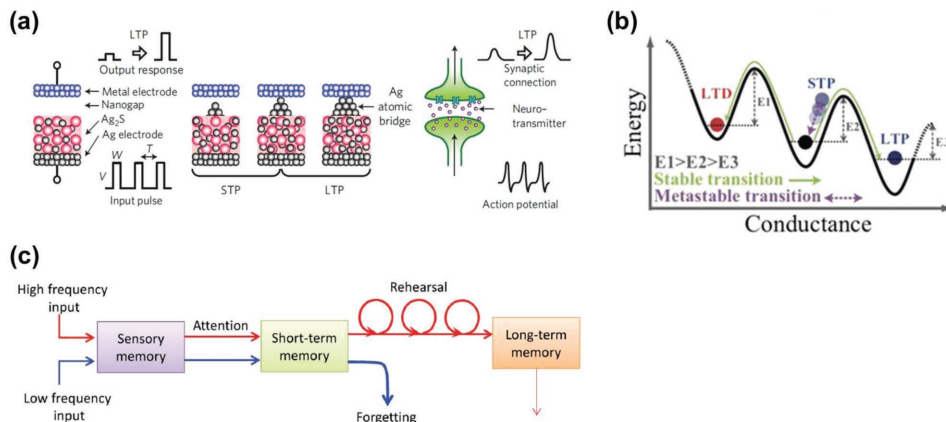


Figure 4. STP and LTP behaviors. a) Schematic diagrams of AgS₂ artificial synapse. When the incomplete and narrow Ag filament is formed, the device is in STP state. On the other hand, when the complete and wide Ag filament is created due to consecutive input pulses, the device state is changed to LTP state. Reproduced with permission.^[67] Copyright 2011, Springer Nature. b) The transition between LTD, STP, and STD, which involve the transition between volatile and nonvolatile state. Reproduced under the terms of the CC-BY 4.0 Creative Commons Attribution 4.0 International License.^[71] Copyright 2016, Springer Nature. c) Data processing sequence in human brain suggested by Atkinson and Shiffrin.^[70] Reproduced with permission.^[45] Copyright 2016, Wiley-VCH.

behaviors according to the history of synaptic plasticity. They obtained metaplasticity on STDP behaviors by WO₃-based artificial synapses. First, five repeated sets of potentiation and depression are induced to the device. Second, three different paired spike sequences are applied to the device. As a result, respectively different STDP behaviors are observed in each case due to the different previous stimuli. In 2017, Zhu et al.^[72] published an article about metaplasticity and demonstrated it as “plasticity of plasticity.” In neuroscience, previous behaviors are important for determining the subsequent synaptic behaviors. Furthermore, Yang et al. in 2017^[73] demonstrated the importance of heterosynaptic plasticity for various synaptic functions such as associate learning and long-term memory (LTM). They achieved the heterosynaptic plasticity by a three-terminal device that contains additional third terminal for controlling the synaptic plasticity between pre- and postsynaptic terminal. Different from homosynaptic plasticity, heterosynaptic devices could separate the enabling terminal and sensing terminal. Also, delicate controls of synaptic plasticity are enabled by the heterosynaptic behaviors.

2.6. Resistive Switching Mechanisms for Artificial Synapses

2.6.1. Classification of Resistive Switching Mechanisms

During the past few years, the working mechanisms of memristors are vigorously investigated for predicting the switching profiles and manipulating them to achieve proper on-off ratio, endurance, retention, and sweep curves.^[53,74] Especially for artificial synapses, the required characteristics are broadened to work sensitively to the input stimulus and generate conductance change without software programming. To achieve the synaptic performance of brain inspired devices, controlling the device conductance became extremely important.^[4,61] Here, two types of working mechanisms of memristors are introduced, namely, filamentary resistive switching and interface type switching, as illustrated in Figure 5.^[57]

2.6.2. Filamentary Resistive Switching

Bipolar filamentary resistive switching of memristors is categorized as electrochemical metallization (ECM) and valence change memory (VCM) according to the electrodes and insulator materials (Figure 5). An ECM SET process is achieved by reduction and electrocrystallization of the metal cations when a positive bias is induced into the top electrode.^[53] Therefore, in most cases, ECM is observed in the top electrodes of electrochemically active metals such as Ag and Cu with insulators of oxides,^[75] perovskites,^[76,77] and organics.^[78] The first observation of a metal filament in ECM was achieved by Hirose and Hirose in 1976.^[79] According to their article, a single Ag filament is observed by micro photographs in Ag/Ag-As₂S₃/Au system. Although there were arguments about the filament whether it is single or multiple, many papers published until the present are coherent with the single-filament switching. Recently, in 2012, Yang et al.^[54] improved this observation in a Ag/SiO₂/Pt system as shown in Figure 6a. They explained the formation of a single-metal filament by the observation of complete and incomplete filaments. As described in Figure 6a(ii), there is only one single filament by the forming process. It is indicated in Figure 6a(iii) that the rupture of the filament occurred by the RESET process at the interface between the inert electrode and the SiO₂ electrolyte material. By long erasing time, the filament is removed in dispersed shape. From this image, it could be predicted that the shape of the filament in LTD state is similar to that in Figure 6a(iii). The thickness of SiO₂ affects the formation of the Ag filament. As indicated in Figure 6a(v), in the longer spacing case, the shape of the filament resembles a dendrite with the branches pointing to the active electrode, whereas in the lower spacing case the shape of filament is cone-like (Figure 6a(ii)). The rupture of filament in the case of short erasing time is shown in Figure 6a(v),(vi). Different from the long erasing time case, there is only a narrow gap between the dielectric and inert electrode interface. Moreover, it could be explained by Figure 6a(iv) that the electric field near the active top electrode is stronger than that of the inert electrode;

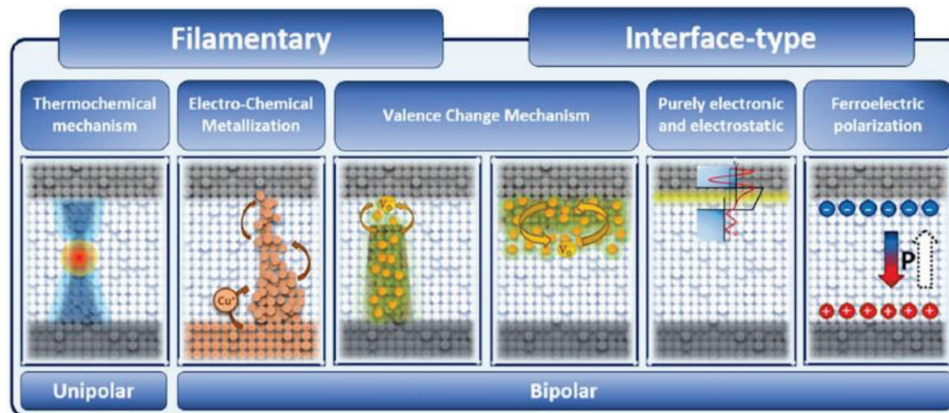


Figure 5. Classifications of demonstrated resistive switching mechanisms. The filamentary type switching includes thermochemical (TCM), electrochemical (ECM), and valence change (VCM) mechanism. The interface-type switching contains VCM, purely electronic and electrostatic effects, and ferroelectric polarization mechanism. The illustrations of each mechanism show how each mechanism works under device operation. Reproduced with permission.^[57] Copyright 2017, Springer Nature.

therefore, the filament near the dielectric/inert interface is thinner than that in the other side. In 2014, Yang et al.^[55] analyzed the formation process type of CFs by a Ag/SiO₂/W structure, which was reproduced by Jeong and Hwang in 2018.^[80] As shown in Figure 6b,e, if the device has both high cation mobility and redox rate, CF starts to be formed from the dielectric/inert interface with a high formation rate. In Figure 6c,f, metal clusters are achieved by low cation mobility and low redox rate from the active/dielectric interface. On the other hand, it is difficult to generate clusters if the cation mobility is high (Figure 6d,g). Therefore, in the case of high cation mobility and low redox rate, the group of clusters generates a dendrite-like filament from the dielectric/inert electrode side. Pan et al. in 2014^[81] also reviewed three types of metal filament formation behaviors in ECM: the formation from inert to active electrode, active to inert electrode, and the middle of a dielectric layer. Similarly, when a device has high cation mobility, a metal filament grows from inert electrode by reduction of active metal cations. On the other way, if cation mobility of a device is low, metal cations migrate a short distance from active electrode before the reduction process by oncoming electrons; thus the metal filament grows from a vicinity of active electrode. Interestingly, Gao et al. in 2013^[82] observed a formation of a metal filament from the middle of the organic layer in Ag/poly(3,4-ethylenedioxythiophene):poly(styrenesulphonate) (PEDOT:PSS)/Pt device. By scanning electron microscopy (SEM) images, they observed the Ag clusters are initially created in the middle of PEDOT:PSS layer by applying 1 V for 2 s, then extended to both electrode by applying constant voltage of 1 V for 4, 10, and 130 s. Pan et al.^[81] discovered that the filament formation behavior is determined by both cation mobility and nucleation energy. If the cation mobility is high, the filament formation starts from inert electrode. According to their simulation, when the nucleation energy decreases under the given cation mobility, the filament formation is changed to start from active to inert electrode. Last but not least, Sun et al. in 2018^[83] also demonstrated the formation of Ag filament in an organic memristors of Ag/CH₃NH₃PbI₃/Pt structure by the transition of Ag atomic concentration in each layer through auger electron spectroscopy (AES) measurement.

Hence, it is possible to adjust the filament growth rate and shape by controlling the cation mobility, redox rate, and nucleation energy. The behavior and characteristics of filament are important for an artificial synapse because the filament change is closely related to the synaptic plasticity appearing as STP, LTP, STD, and LTD.

The VCM mechanism is normally created in the structure sandwiched between the resistive layer and inert metal electrodes.^[74] The resistive layer is normally a transition metal oxide such as binary metal oxides (HfO_x,^[84] TaO_x,^[85] and ZnO^[86]), and perovskites such as BiFeO₃^[87] and SrTiO₃.^[88] Different from ECM, the CF consists of ion vacancies.^[53] To generate oxygen vacancies, the electrode should work as an oxygen reservoir by occupying oxygen ions from oxides and storing them in the reservoir. By applying a reverse bias, the oxygen vacancies move toward the oxygen reservoir and are annihilated.^[80] In 2009, Yang et al.^[74] observed a CF that consists of oxygen vacancies with a Pt/TiO₂/Pt device. They postulated that when a positive bias is induced on the top electrode, oxygen ions with negative charge will drift toward the top electrode and will be discharged to generate O₂ gas at the anode. The gas bubbles are observed near the top electrode when a positive bias is applied on it. When the bias is removed, the bubbles also disappear immediately. In addition, they also observed the oxygen vacancy filament by a local pressure-modulated conductance microscopy (LPCM). By LPCM measurement, an atomic force microscopy (AFM) tip scans the surface while a small \approx 50 mV bias is induced on the electrodes, and the current is measured. The oxygen vacancy channel is locally formed at the oxide/anode interface when the forming is on, whereas it is collapsed when the forming is off. While oxygen vacancies form and move toward the cathode achieving a localized CF, O²⁻ ions drift in the direction of the anode and are discharged, achieving physical deformation. In 2010, Kwon and co-workers^[89] also successfully observed nanofilaments in Pt/TiO₂/Pt device during resistive switching and investigated the change of atomic structure in the filament formation region. As shown in Figure 7a, they fabricated a Pt/TiO₂/Pt device and applied a negative voltage to the top electrode. Blown-off parts in the Pt top electrode are

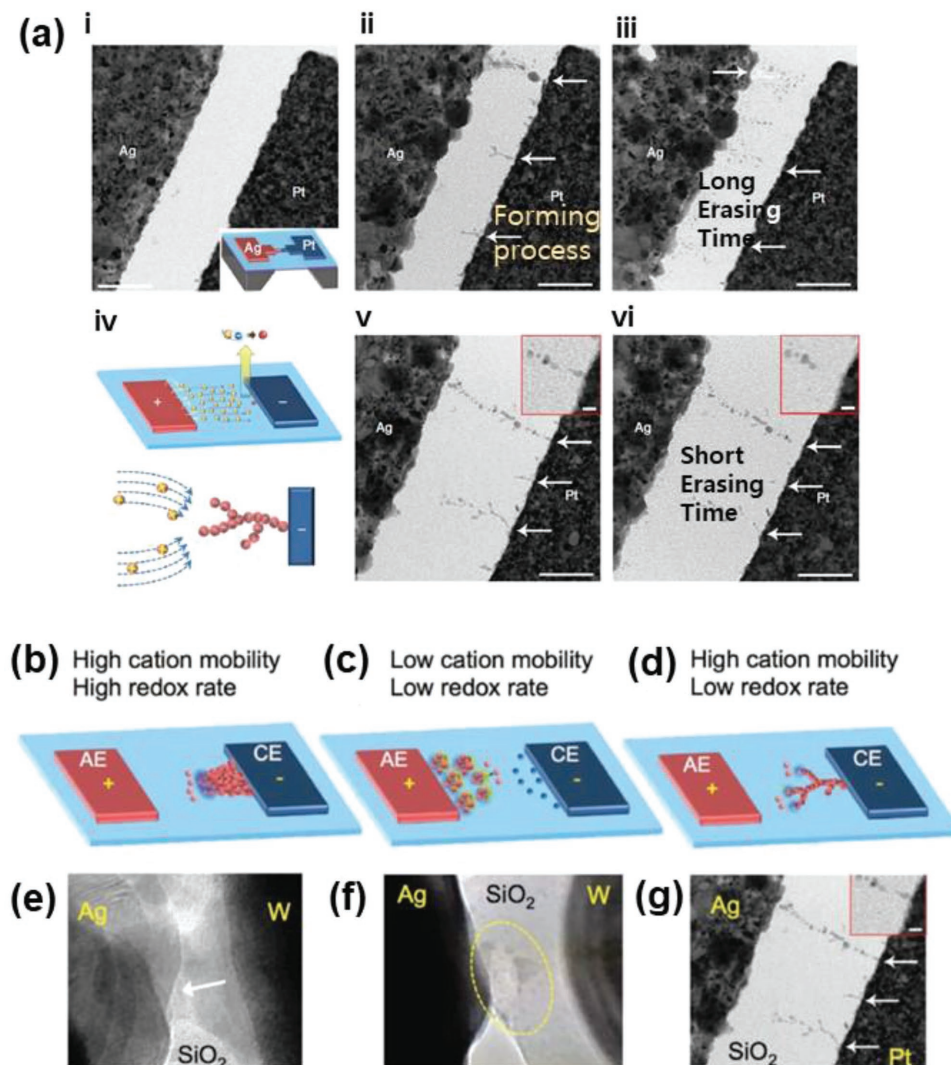


Figure 6. TEM images of formation and rupture of Ag conducting filaments (CFs) in SiO_2 -based memristors. a-i) TEM images of as-fabricated two-terminal SiO_2 -based memristors. Scale bar: 200 nm. a-ii) TEM image which approve the shape of Ag CFs under the process of forming. Single perfect Ag filament is created and several incomplete filaments are observed. Scale bar: 200 nm. a-iii) TEM image of a rupture of the filament under the opposite bias with long duration time. The Ag CF is fully dispersed. Scale bar: 200 nm. a-iv) Illustrations of the filament formation process displaying the migration and reduction of Ag cations. a-v) TEM image of the same structure with larger thickness of SiO_2 after the Ag CF forming process. It shows the similar profiles with (a-ii). Scale bar: 200 nm. a-vi) TEM image of a rupture of the filament in (a-v) under the opposite bias with short duration time. The small disconnection with the Pt bottom electrode is observed, and the filament is still remained. Scale bar: 200 nm. Reproduced with permission.^[54] Copyright 2012, Springer Nature. b) A schematic diagram of the filament formation under the condition of high cation mobility and high redox rate. The CF grows from the bottom electrode side by reduction process of metal cations. c) A schematic diagram of the filament formation under the condition of low cation mobility and low reduction rate. Metal clusters are observed near the top electrode. d) A schematic diagram of the filament formation under the condition of high cation mobility and low redox rate. Group of clusters generate a branch-like filament from the bottom electrode side. e) TEM image of $\text{Ag}/\text{SiO}_2/\text{W}$ memristors which shows a profile of Ag CF in the case of (b). f) TEM image of the same device with (e), which shows a profile of Ag CF in the case of (c). Reproduced with permission.^[55,80] Copyright 2014, Springer Nature, and Copyright 2018, Wiley-VCH. g) The same TEM image with (a-v) in the case of (d). Reproduced with permission.^[54] Copyright 2012, Springer Nature.

generated by strong filament formation during SET process and observed by SEM as shown in Figure 7b. The generation of blown-off region is possibly caused by the abrupt evolution of compressed excessive oxygen gases. They also found that the considerable amount of TiO_2 film is changed to $\text{Ti}_{n-1}\text{O}_{2n-1}$ after resistive switching and observed it by high-resolution transmission electron microscopy (HRTEM). As shown in Figure 7c, a conical shape of filament that connects the top and bottom

electrode is observed in the SET state. By calculation of d -spacing, they discovered that the atomic structure of filament region is changed to Ti_4O_7 . The filament profile of RESET state is also suggested in Figure 7d. In RESET state, the conical-shaped filament is disconnected from the Pt bottom electrode.

Furthermore, VCM could be applied for organic-inorganic halide perovskites. In 2018, Hwang and Lee^[90] fabricated a $(\text{CH}_3\text{NH}_3)_3\text{Bi}_2\text{I}_9$ with Au and indium tin oxide (ITO) electrodes,

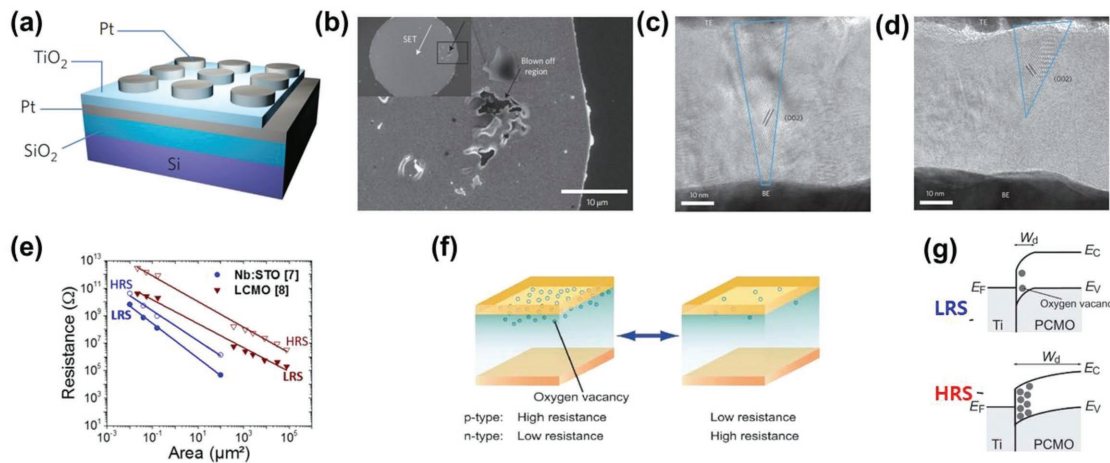


Figure 7. Observation of filaments composed of oxygen vacancies and schematic explanations of interface type switching. a) A structure of Pt/TiO₂/Pt device. b) SEM images of blown-off region in the Pt top electrode generated in SET state. c) A HRTEM image of a filament region in SET process. The atomic structure of filament region is changed from TiO₂ to Ti₄O₇. d) A HRTEM image of the disconnected filament in RESET state. Reproduced with permission.^[89] Copyright 2010, Springer Nature. e) Dependence between the device area and resistance in interface type resistance switching devices of Nb:STO and LCMO. The resistance is inversely proportional to the device area. Reproduced with permission.^[57] Copyright 2017, Springer Nature. f) Schematic diagrams of changes in the density of oxygen vacancies near the interface between dielectric/top electrode and the device resistance state according to the type of the oxide. The resistance state of the interface type switching memories is decided by the density of oxygen vacancies. g) Band diagram of a p-type oxide, PCMO, and a Ti top electrode according to the resistance states of LRS and HRS. The W_d between the Ti electrode and PCMO is changed according to the polarity of the bias and switch the resistance state. Reproduced with permission.^[56] Copyright 2008, Elsevier.

and showed its electrical properties as a memristor. They explained that the working mechanism is VCM by formation of iodide vacancies filament. In fabricating VCM-based memristors for brain-inspired devices, controlling the formation rate and shape of the ion vacancy filament is the key to achieve a gradual resistance change and synaptic plasticity such as LTP, LTD, STP, and STD.

Interestingly, Sun et al. in 2018^[83] discovered a new behavior of resistive switching mechanism by observing the coexistence of metallic and vacancy filaments in a Ag/CH₃NH₃PbI₃/Pt structure. If the thickness of CH₃NH₃PbI₃ is ≈300 nm, the Ag filament could not be completely formed because of the large gap between the top and bottom electrode. At the same time, iodine vacancy (V_I) is generated by the applied voltage because the activation energy of I⁻ is the smallest among I⁻, Pb²⁺, and CH₃NH₃⁺. Therefore, resistive switching is occurred by VCM. However, if the thickness of CH₃NH₃PbI₃ is ≈90 nm, complete Ag and V_I filaments are formed. Since the conductivity of a Ag filament is much larger than a V_I filament, the resistive switching is dominantly generated by Ag filament, which is called ECM. They employed AES measurement to approve the demonstration.

2.6.3. Interface-Type Resistive Switching

Interface-type switching is generated by a physical or chemical phenomenon at the dielectric and electrode interface.^[57] It is also included in the VCM mechanism type (Figure 5). In this case, the device resistance is inversely proportional to the electrode area as shown in Figure 7e. It is known that different from the filamentary type, the interface type switching generally does not require a forming step, and it easily obtains a multilevel storage because it changes the resistance state by

a uniform interface effect.^[53,57] Overcoming the electroforming randomness of memristors, devices could achieve reproducibility and cell to cell uniformity.^[91] In 2008, Sawa^[56] published an article about an interface-type resistive switching mechanism. According to the article, the contact resistance between the dielectric layer and metal electrodes is originated mostly by a Schottky barrier. If the dielectric layer consists of p-type oxides such as Pr_{0.7}Ca_{0.3}MnO₃ (PCMO), the decrease in metal electrode work function arouses an increased contact resistance at the interface between the metal and dielectric. By contrast, when the dielectric material is an n-type oxide such as SrTi_{0.99}Nb_{0.01}O₃ (Nb:STO), the increase in metal work function generates an increase in contact resistance. In the conventional Schottky model, the capacitance equation is given by $C = \frac{\epsilon_0 \epsilon_s S}{W_d}$, where W_d is the width of the depletion layer, ε₀ is the relative dielectric constant of a vacuum, ε_s is the semiconductor relative dielectric constant, and S is the cell area. This equation indicates that LRS is achieved by tunneling through the Schottky barrier with a narrow W_d, while HRS is created by inhibited tunneling at the Schottky barrier with a wide W_d. By adjusting the work function of the metal electrodes or electronic properties at the vicinity of metal/dielectric interface, the conductance of the device could be controlled. As illustrated in Figure 7f, the density of oxygen vacancies affects the resistance state of the device. Oxygen vacancies in p-type oxides work as acceptors; thus, the reduction at the interface could generate a narrow W_d. In the p-type oxide PCMO case, the oxygen vacancies are removed by a reduction process, and the number of oxygen vacancies is decreased; then W_d becomes narrow, generating LRS (Figure 7f,g). By contrast, the oxygen vacancies in n-type oxides work as donors so that the reduction process at the interface causes an increase in W_d and decrease in the device conductance (Figure 7f).

3. Metal Oxides

3.1. Binary Oxides

Recently, the most actively researched binary oxide materials for electronic synapses are HfO_x ,^[11–16,84] TaO_x ,^[17,18,85] WO_x ,^[19–21,59] and ZnO ,^[86,92,93] which facilitate in achieving scalability and a simple structure. Because binary oxides are conventional materials for resistive switching memories, there are many reports about binary oxide-based electronic synapses. **Table 1** provides a summary of electrical and synaptic properties of oxide-based memristors. As mentioned above, there are three main requirements for memristor-based artificial synapses: low power consumption, high data transfer speed, and scalability. Among those reports, Yu et al.^[94] published an article in 2011 about an electronic synapse with a $\text{TiN}/\text{HfO}_x/\text{AlO}_x/\text{Pt}$ structure achieving a low energy consumption of less than 1 pJ for the first time in a two-terminal electronic synapse (**Figure 8a**). Because memristors made of HfO_x -based materials have shown a high memory performance by achieving high speed, endurance, and retention, and AlO_x -based memristors have achieved low energy consumption, they decided to fabricate a bilayer structure of $\text{HfO}_x/\text{AlO}_x$. The resistance changes between HRS and LRS occur by oxygen vacancies filament mean synaptic strength modifications. In **Figure 8b**, by gradually increasing the compliance current through the application of a positive voltage, the current of the current–voltage (*I*–*V*) sweep is gradually increased to LRS without overlapping with the previous sweep. Furthermore, by gradually decreasing the compliance current while inducing a negative bias, the current of *I*–*V* sweep is gradually reduced to HRS without overlapping with the former sweep. In the pulse cycling with a narrow pulse width of 50 ns, it is shown in **Figure 8c** that continuously increasing five RESET pulses from –2.2 to –2.6 V facilitates a gradual increase in resistance to HRS. Then following a gradually increased SET pulse from 1.4 to 1.8 V generates a gradual decrease in resistance to LRS. Even after 10^5 cycles, the gradual increase and decrease in resistance are executed by the input pulse change. Low energy consumption and fast switching, which are important for an artificial synapse, are observed in this device (**Figure 8d**). By applying a +1.5 V with 50 ns input pulse, the current amplitude increases only after 30 ns and the consumed energy is only 50 pJ calcu-

lated by integrating the voltage, time, and current. Moreover, for the first learning rule, STDP is facilitated by this device. As explained in Section 2.2, synapses receive spikes from different neurons and prespikes and postspikes are allowed with opposite directions to synapses. For the first learning rule, the gap between each spike timing is the main parameter for changing the synaptic strength. By successful programming pulses, they achieved an STDP graph (**Figure 8e**) similar to that of biological synapses (**Figure 3c**). These results indicate that $\text{HfO}_x/\text{AlO}_x$ -based memristors could be a possible candidate for artificial synapses.

Supported by conventional studies on oxide memristor-based artificial synapses, researchers tend to concentrate on the methods of controlling the CF. In 2016, Niu et al.^[14] suggested a nanotip engineering for geometric CF confinement with a $\text{TiN}/\text{Ti}/\text{HfO}_2/\text{CoSi}_2/\text{Si}$ nanotip-based memristor. According to their report, the confined CF is formed because only a limited amount of Ti and CoSi_2 could be oxidized from the nanotip to its vertical direction. As shown in **Figure 8f**, only the interface between the Si nanotip and HfO_2 could be oxidized when a negative bias is induced to the top electrode. Then, the filament grows from the oxidized nanotip top to the Ti/TiN top electrode vertically. This is because of the localized electric field and ionic current density confinement. Although the authors showed only the memristor properties such as the *I*–*V* sweep, endurance, and retention, this technology could be applied for electronic synapses by controlling the size and number of CFs.

Furthermore, in 2016, Wang et al.^[95] tried to modulate CFs by a compliance current change. They fabricated a $\text{Pt}/\text{FeO}_x/\text{Pt}$ structure on a 1 μm thick SiO_2 layer (**Figure 9a**). When the smallest compliance current of 0.1 mA is applied on the device, the weak and narrow pyramidal shape of CF is formed by a small amount of oxygen vacancies similar to that in **Figure 9b(i)**. This could be the reason that its *I*–*V* sweeps are overlapped with each other as observed in **Figure 9c(i),(ii)**. When the compliance current becomes larger than 0.5 mA, the CF also becomes wider, creating a conical shape, as illustrated in **Figure 9b(ii)**, because of the increased amount of oxygen vacancies. As a result, the *I*–*V* sweeps for this case did not overlap with each other (**Figure 9c(iii),(iv)**). When the largest compliance current of 1 mA is applied on the device, a wide and cylinder-like filament is formed as shown in **Figure 9b(iii)**.

Table 1. Summary of electrical switching and synaptic properties of oxide-based memristors.

Structure	Device thickness [nm]	Switching mechanism	V_{set} [V]	V_{reset} [V]	Potentiation and depression	On/off ratio	Endurance	Ref.
TiN/ $\text{HfO}_x/\text{AlO}_x/\text{Pt}$	AlO_x : 5/ HfO_x : 5	Filamentary (VCM)	≈1.5	–1	O	>10 ³	10 ⁵	[94]
TiN/ $\text{SiO}_2/\text{TaO}_x/\text{Pt}$	TaO_x : 25	Filamentary (VCM)	≈0.5	–0.5	O	–	10 ⁶	[17]
Ag/ HfO_x/Pt	HfO_x : 10	Filamentary (ECM)	0.21–0.37	–0.1 to 0.15	O	>10 ³	–	[11]
TaN/ HfO_x/Pt	HfO_x : 10	Filamentary (VCM)	1.3–1.8	–1.3 to 1.5	O	>10 ²	10 ⁴	[11]
TiN/ HfO_2/TiN	HfO_2 : 6	Filamentary (VCM)	≈1.5	–1.5	O	–	–	[13]
TiN/ $\text{HfO}_2/\text{Ti}/\text{TiN}$	HfO_2 : 6/ Ti : 15	Filamentary (VCM)	≈1	–1.1	O	–	–	[16]
Al/ $\text{ZnO}/\text{Ta}_2\text{O}_5/\text{ITO}$	ZnO : 40	Interface type	–	–	O	10 ⁵ –10 ⁶	–	[86]
W/ TaO_x/Pt	TaO_x : 80	Filamentary (VCM)	≈2.5	–1.5	–	≈10 ²	≈10 ⁴	[85]
Al/ WO_x/Cu	WO_x : 50	Filamentary (VCM)	≈1.1	–0.9	–	≈10 ⁴	10 ³	[20]

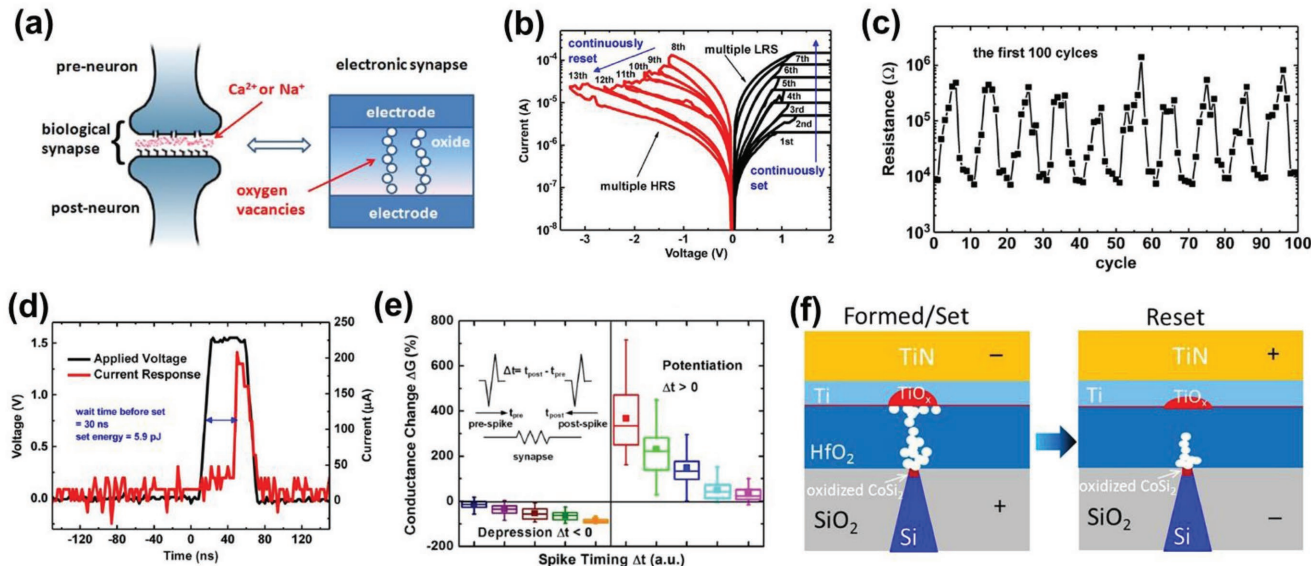


Figure 8. Synaptic behaviors of binary oxide electronic synapses. a) Comparison between a biological synapse and an artificial synapse. In binary oxides synapses, the top and bottom electrodes work as pre- and postneuron. The oxygen vacancies filaments emulate neurotransmitters where the electrical signals could be transported. b) I - V sweeps of HfO_x/AlO_x synaptic device in analog type switching. By gradually changing current compliance, the I - V sweep is gradually increased or decreased without overlapping with previous sweeps. c) The potentiation and depression behaviors with pulse type biases. d) Low energy consumption of HfO_x/AlO_x synaptic device. After applying +1.5 V during 50 ns, the current amplitude rises consuming only 50 pJ. e) STDP behaviors of the same device. If $\Delta t > 0$, the device is in potentiation state while $\Delta t < 0$, it is in depression state. Reproduced with permission.^[94] Copyright 2011, IEEE. f) Schematic diagrams of the formation and rupture of oxygen vacancies filament in a $TiN/Ti/HfO_2/SiO_2$ device with a Si-nanotip. Confined area of the interface between Si-nanotip and HfO_2 is oxidized and generates a conducting filament. When a positive bias is applied to the top electrode, the filament is ruptured. Reproduced under the terms of the CC-BY Creative Commons Attribution 4.0 International License.^[14] Copyright 2016, Springer Nature.

In this cylindrical case, the formation and rupture of CF could occur in the middle of the filament. The I - V sweeps are also gathered with increasing current level and not overlapping with each other as well (Figure 9c(v),(vi)). It is also observed that with increasing compliance current, the retention is also increased.

Wang et al. in 2016^[96] demonstrated diffusive dynamics of memristors consists of two inert electrodes and a dielectric layer with Ag nanoclusters, which emulate Ca^{2+} dynamics in biological synapses. They fabricated $Au/SiO_xNy:Ag/Au$ structure and

observed Ag migration from 0.1 to 5 s by in situ TEM. By the migration of Ag clusters, synaptic behaviors of STDP, potentiation, and depression are achieved.

3.2. Oxide Heterojunctions

Recently, metal oxide-based memristors tend to be heterostructured with two different dielectric materials to control electron

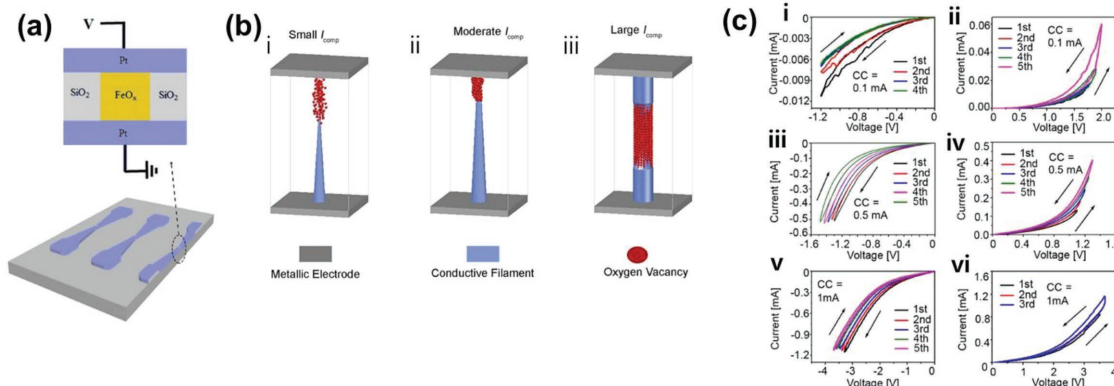


Figure 9. Control of conducting filament for neuromorphic applications in $Pt/FeO_x/Pt$ device. a) Schematic illustrations a $Pt/FeO_x/Pt$ device structure. b) Illustrations of the shape of conducting filaments according to the different compliance current (I_{comp}). c) I - V sweeps of the $Pt/FeO_x/Pt$ device with different I_{comp} of 0.1 mA (i, ii), 0.5 mA (iii, iv), 1 mA (v, vi). When the I_{comp} is 0.5 mA, the I - V sweeps obtain gradual increase and decrease without overlapping, which is the best condition for neuromorphic applications. Reproduced under the terms of the CC-BY Creative Commons Attribution 4.0 International License.^[95] Copyright 2016, Springer Nature.

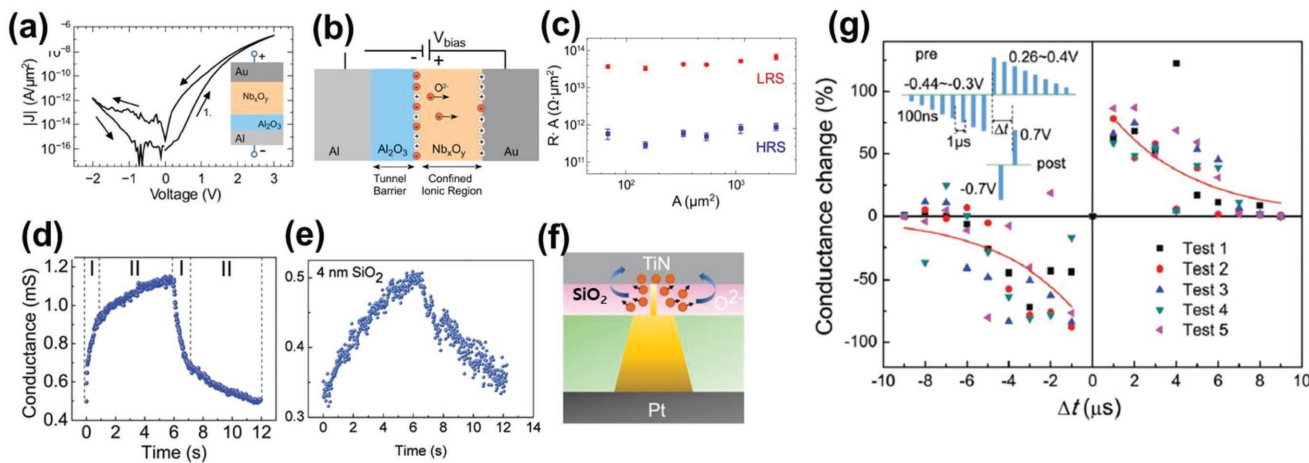


Figure 10. Synaptic behaviors of oxide heterojunction devices. a) A graph of absolute current density $|J|$ versus applied voltage (V) in an $\text{Al}/\text{Al}_2\text{O}_3/\text{Nb}_x\text{O}_y/\text{Au}$ double barrier memristors. It shows broaden hysteresis. b) A schematic diagram of $\text{Al}/\text{Al}_2\text{O}_3/\text{Nb}_x\text{O}_y/\text{Au}$ device where Al_2O_3 works as a tunnel barrier and Nb_xO_y works as a confined ionic region. c) The area-resistance values versus junction-area in the same device which works by the interface type switching. Reproduced under the terms of the CC-BY Creative Commons Attribution 4.0 International License.^[91] Copyright 2015, Springer Nature. d) A nonlinear conductance changes versus time graph of $\text{TiN}/\text{TaO}_x/\text{Pt}$ device without SiO_2 DLL layer. e) A linear conductance changes versus time graph of $\text{TiN}/\text{TaO}_x/\text{Pt}$ device with SiO_2 DLL. f) A schematic diagram of controlled filament growth process in $\text{TiN}/\text{TaO}_x/\text{Pt}$ through SiO_2 DLL. g) A STDP behavior of $\text{TiN}/\text{SiO}_2-1 \text{ nm}/\text{TaO}/\text{Pt}$ device which follows asymmetric Hebbian learning rule with programmed pre- and postpulses. Reproduced with permission.^[17] Copyright 2016, RSC Publishing.

tunneling^[91] or ion diffusion rate,^[17] which are related to device conductance. In 2015, Hansen et al.^[91] published an article about $\text{Al}/\text{Al}_2\text{O}_3/\text{Nb}_x\text{O}_y/\text{Au}$ double-barrier memristors that change the resistance state by an interfacial reaction, where the amorphous Al_2O_3 works as a tunnel barrier and Nb_xO_y acts as an ionic conductor (Figure 10b). Oxygen vacancies are confined in Nb_xO_y , and the Al_2O_3 layer constrains the electron tunneling to generate a gradual interfacial switching (Figure 10a). The amount of oxygen vacancies in Nb_xO_y region determines the conductance, and the oxygen vacancies are drifted to the $\text{Al}_2\text{O}_3/\text{Nb}_x\text{O}_y$ (tunnel barrier) interface or $\text{Nb}_x\text{O}_y/\text{Au}$ (Schottky barrier) interface according to their charge and mobility. Then they are redistributed to the original state by applying an opposite bias. The area-dependent resistance change is provided to prove the interfacial switching (Figure 10c). By the homogeneous change of resistance state through the interface reaction, the conductance of the device could gradually increase or decrease, avoiding abrupt changes and the electroforming step, which is one of the important properties of artificial synapses.

In addition, in 2016, Wang et al.^[17] published an article that shows the control of filament growth and dissolution rate by forming an ion diffusion limiting layer (DLL) of SiO_2 at the TiN/TaO interface. Moreover, the SiO_2 layer contributes to a low energy consumption through a narrow filament size because of its dense microstructure. The $\text{Pt}/\text{TiN}/\text{SiO}_2/\text{TaO}_x/\text{Pt}$ structure is fabricated in a cross-bar structure. It is known that a TiO_x layer contains many oxygen vacancies to create CF, where the TiN layer acts as an oxygen reservoir. By inducing 1 V with 100 ns input pulses, they monitored the potentiation and depression curve by the conductance versus time without the SiO_2 DLL (Figure 10d). The linearity of the potentiation and depression curve is important for artificial synapses because it represents the uniform change rate of conductance when the same amplitude or width of input pulses is applied continuously. Referring

to Figure 10d, region I indicates a rapid growth of CF limited by the redox reaction. After the reduction reaction with adjacent ions, the reduction reaction with farther ions occurs and the rate is determined by ion diffusion in region II. Because decreasing the number of ions is normally impossible, they decided to enlarge region II to make a more linear increase by inserting the DLL. Because of adding a more insulating SiO_2 layer, the formation and rupture of CF occurred at the SiO_2 layer (Figure 10f). The oxygen vacancies are attracted to the SiO_2 layer by applying a positive bias to the TiN top electrode while the oxygen ions are drifted to the SiO_2 layer from the TaO_x layer. Thus, the abrupt conductance change could be inhibited and a gradual increase in conductance could be implemented. When the SiO_2 thickness is 4 nm, the linearity of the conduction curve rises as shown in Figure 10e. In addition, an STDP that is similar to that of a biological synapse could be achieved with this device (Figure 10g).

Imitation of Ca^{2+} dynamics with oxide heterojunction memristors is also published by Kim et al. in 2015.^[97] They demonstrated a second-order memristor with $\text{Pd}/\text{Ta}_{2-\chi}/\text{TaO}_y/\text{Pd}$ device. In a second-order memristor, the secondary-state-variables emulate Ca^{2+} ions in biological synapses that indirectly effect on the synaptic weight. By this process, synaptic behaviors of STDP, potentiation, and depression are obtained without pulse programming.

3.3. Amorphous Oxide Semiconductors and Perovskite Oxides

3.3.1. Amorphous Oxide Semiconductors

The amorphous InGaZnO (α -IGZO) has superior advantages compared to crystal materials. It has high uniformity, room-temperature growth conditions, easy to control electrical

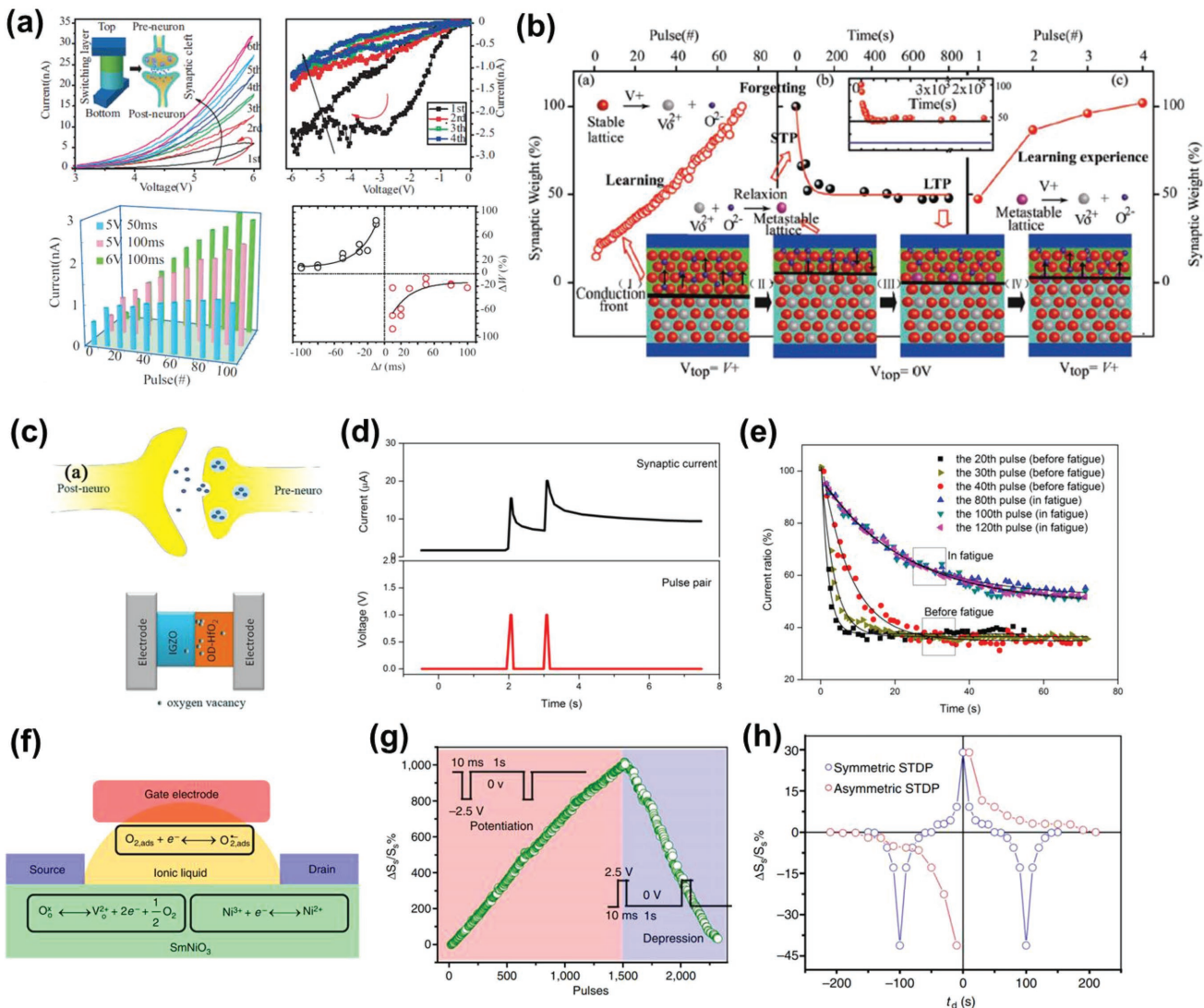


Figure 11. Device structures and synaptic behaviors of amorphous oxide (IGZO), oxide heterojunction (IGZO-HfO₂) and perovskite oxide synapses. a) I - V sweeps, SRDP, and STDP behaviors of Pt/α-IGZO/Pt memristors. The I - V sweeps are gradually increased without overlapping. The STDP behaviors follow asymmetric anti-Hebbian learning rule. The SRDP behaviors are gathered by different pulse amplitudes and widths. b) Schematic diagrams of oxygen migrations and learning experiences in Pt/α-IGZO/Pt memristors. After the first linear learning experience, synaptic weight is still remained in certain level. So, the second learning process gains the 100% synaptic weight with only four input pulses. Reproduced with permission.^[98] Copyright 2012, Wiley-VCH. c) A device structure of IGZO-HfO₂-based artificial synapse. d) Synaptic paired pulse facilitation (PPF) behavior of the IGZO-HfO₂ device. The second pulse is triggered by the first pulse. e) The current decay curves according to the different number of input pulses. Reproduced under the terms of the CC-BY Creative Commons Attribution 4.0 International License.^[103] Copyright 2017, Springer Nature. f) The structure of a three-terminal perovskite oxide, SmNiO₃, synapse. g) Linear potentiation and depression behaviors with programmed pulses in the SmNiO₃ synapse. h) The symmetric and asymmetric STDP behaviors of the SmNiO₃ synapse by programmed source spikes. Reproduced with permission.^[22] Copyright 2013, Springer Nature.

properties, low energy consumption, and remarkable flexibility. Because it does not have grain boundaries (GBs), it can be easily scaled down for high-density artificial synapses.^[98,99] In 2012, Wang et al.^[98] reported an article about α-IGZO memristor (Pt/α-IGZO/Pt)-based artificial synapses in which the mechanism is based on the oxygen concentration-gradient-induced ion diffusion. By applying a positive bias to IGZO, the oxygen-rich layer and the oxygen ions are compressed to the top electrode by increasing the device conductance. When the bias is stopped, the oxygen ions are drawn back to the bottom electrode

side, reducing the device conductance (Figure 11b), which could be considered as a type of interface switching. As shown in Figure 11a, this α-IGZO memristor achieves a gradual current increase by positive bias voltages and a gradual current decrease by negative bias voltages. Moreover, it fulfills SRDP by pulse width and amplitude changes. When the pulse amplitude is 5 V and the width is 50 ms, the current increasing rate is almost saturated after 40 pulses. However, when the pulse width is increased to 100 ms, the current increasing rate is larger than the previous condition. When the pulse amplitude is increased

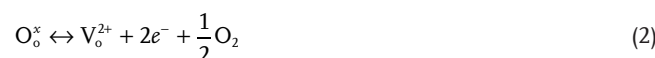
to 6 V, the current increasing rate becomes even larger. Moreover, STDP is also observed in this device, which follows the asymmetric anti-Hebbian learning rule. An interesting learning behavior is also achieved by this device as shown in Figure 11b. The first learning process requires \approx 80 pulses to fulfill the synaptic weight of 100%. In comparison, the second learning rule achieves the same synaptic weight of 100% with only four pulses. It means that the second learning rule is easier than the first, which is similar to the human memory. Furthermore, two terminal IGZO-based synaptic transistors are highly researched by fabricating an electric-double-layer (EDL) unit.^[99–102] In 2015, Zhou et al.^[99] fabricated three-terminal transistors with IGZO channel on ITO substrate and InZnO (IZO) source and drain. It does not require a bottom conductive layer; thus, the IGZO channel could be linked to the induced gate voltage.^[100] They achieved a low energy consumption of \approx 0.23 pJ per spike and EPSC.

The heterojunction structure with IGZO as the oxygen-rich layer and HfO₂ as the oxygen-deficient film is also fabricated as a synaptic memristor by Jiang et al. in 2017.^[103] They generated the Al/HfO₂/IGZO/Au structure as shown in Figure 11c. The device obtained a paired pulse facilitation (PPF), which means that the current is increased by the second pulse rather than the first pulse. In other words, the first pulse affects the second pulse by maintaining a certain level of current after the pulse is removed (Figure 11d). Furthermore, as shown in Figure 11e, the forgetting behavior is observed. Compared to the 20th pulse case, when the 40th input pulse is applied, the device has a slower decreasing rate, which is referred to as SRDP. Moreover, it is shown that above the 80th pulse case, a fatigue process is experienced, which fulfills the high retention time in the higher current level (Figure 11e). There is a threshold pulse number for the long retention time. The mechanism of this device is an interface type related to the oxygen content in the IGZO layer similar to the two-terminal device as mentioned above. When the positive bias is induced to the top electrode, the oxygen ions compress the IGZO film, increasing the device conductance. This process determines the thickness of the oxygen-rich layer and oxygen-deficient layer, which is a key parameter of the device conductance. By contrast, when the bias is off, the oxygen ions are drawn back as the ion content gradient decreases. It is shown that the second pulse achieves more compressive oxygen ions than the first pulse, because the ions have not fully returned to their original location. This phenomenon could explain SRDP, STP, and LTP. When the pulse idle time is short, the oxygen content gradient maintains an increased amount and the conductance keeps increasing with respect to LTP. In HfO_x, which is the oxygen-deficient layer, clustered oxygen ions are scattered and generate a CF when the positive pulse is applied on the top electrode. If it is removed, the filament changes back to a cluster shape as shown in Figure 11f.

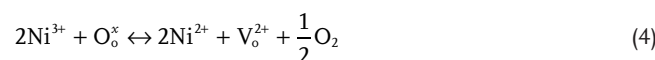
3.3.2. Perovskite Oxides

Perovskite oxides such as SmNiO₃^[22] (SNO), BiFeO₃^[23–25,87] (BFO), SrTiO₃ (STO),^[88] and SrRuO₃^[104] have been researched for memristor and memristor-based synapses for the past few

years. They have advantages of excellent localized accumulation of oxygen ions and can easily convert a defective structure, and the switching mechanism is generally the interface type. In 2012, Mayr et al.^[24] fabricated a Pt/BFO/Au structure and obtained the STDP curve. Moreover, in 2013, Cederström et al.^[25] created the same structure and showed the STDP curve. Different from two-terminal artificial synapses, Shi et al.^[22] successfully fabricated three-terminal artificial synapses with SNO as a channel material (Figure 11f). Conventional two-terminal electronic synapses separate the stimulus transmission and learning process. However, three-terminal devices could combine the two processes at the same time; therefore, they could provide a novel solution for efficient synaptic devices. In the three-terminal synaptic transistor, the source and drain emulate the preneuron and postneuron. As shown in Figure 11f, the two major reactions are displayed as



Hence, the overall chemical reactions are



By applying a 10 ms width and -2.5 V amplitude input pulses on the gate, the synaptic weight increases, obtaining potentiation by each pulse with 1 s of pulse idle time. After 1500 potentiation pulses, input gate pulses of 10 ms width and 2.5 V amplitude generate depression with the same pulse idle time (Figure 11g). The symmetric and asymmetric STDP curves are also detected. As shown in Figure 11h, the change in sheet conductance is monitored as an asymmetric Hebbian learning rule when the drain spike preceded the source spike. By contrast, if the source spike preceded the drain spike, the STDP behavior follows a symmetric Hebbian learning rule. They also determined the influence of gate channel distance, temperature, gate bias voltage, and duration on the device resistance.

4. Organic Materials

4.1. Polymers

Memristors with inorganic semiconductors have a limitation to emulate diverse functions of the human brain due to their uncontrollable filament and ion migration. In other words, they could emulate only partial functions of the human brain. In addition, they contribute to environmental problems owing to their toxicity, and some of them require a high cost. Recently, polymers are highlighted as promising candidates for bioinspired electronics, which surpass inorganic memristors. Polymer materials have excellent properties as memristor materials because they could be manufactured at low cost and fabricated by simple solution processes. Furthermore, they can facilitate flexible devices by their excellent ductility, and they can achieve compatibility with the CMOS technology. In addition, it is easy to modulate their electrical performance by a designed

molecular synthesis.^[105] Moreover, organic materials can easily achieve low power consumption, high accuracy, and biocompatibility.^[26] In 2014, Chen et al.^[105] published a review article about polymer-based resistive random access memory and artificial synapses. They mentioned that the resistive switching mechanism of polymers is different from Si-based technologies. Polymer-based memristors change their conductance by changing their intrinsic properties through redox reaction, phase and conformation change, and charge transferring.

The first polymer-based memristors were proposed by Banerjee et al. in 2011.^[27] They fabricated a cobalt(III)-containing conjugated (CP) and nonconjugated polymer (NCP) with an azo-aromatic backbone by solution processes. They monitored the cyclic voltammograms (CV) of CP, NCP, and Ag/AgCl reference electrodes, and then revealed that the first electronic reaction is caused by the reduction from Co (III) to Co (II). They observed HRS and LRS with bipolar switching in the *I-V* curve and the hysteresis difference between CP and NCP groups. The CP groups show a wider gap of resistance change. In addition, they obtained an on-off ratio of 10^2 for CP and under 10 for NCP, an endurance of 10^4 cycles, and a retention of $\approx 10^4$ s by the CP device.

After the first polymer artificial synapses, other polymer materials have been consistently reported owing to their flexibility, simple fabrication process, and added functionalities. Among the polymer materials, PEDOT:PSS is actively researched because it is easy to modify its conductivity by diverse

parameters. In 2013, Li et al.^[28] constructed Ag/PEDOT:PSS/Ta two-terminal electronic synapses as shown in Figure 12a. They successfully imitated synaptic plasticity including gradual SET and RESET, linear potentiation and depression (Figure 12b), SRDP (Figure 12c), and STDP (Figure 12d). Because they defined Δt as the time interval of prespike and postspike, the device shows a synaptic weight increase when $\Delta t < 0$. The programmed pulse contains positive and negative pulses at the same time; thus, the synaptic weight is maximum when $\Delta t = \pm 50$ ms (Figure 12d). In addition, they clearly showed that the highest frequency input pulses of 10 Hz generate a faster current change rate than other conditions, which represent an SRDP behavior (Figure 12c). Moreover, they revealed that the resistive switching mechanism of this device is the filamentary ECM type by cross-sectional TEM images. The Ag filament is clearly formed compared to the pristine state in the TEM images, and the EDX profile shows the increased peak of Ag elements near the Ta electrode. Three-terminal organic artificial synapses with PEDOT:PSS were explored by van de Burgt et al. in 2017.^[26] They utilized the PEDOT:PSS as the presynaptic electrode, and a poly(ethylenimine) (PEI)/PEDOT:PSS as the postsynaptic electrode. When a positive input bias is applied to the presynaptic electrode, cations from the PEDOT:PSS drift to the postsynaptic electrode and simultaneously protonate the PEI. Then electrons could pass through this external circuit and the device conductance is increased. Additionally, they obtained potentiation and depression conductance change curves, and a

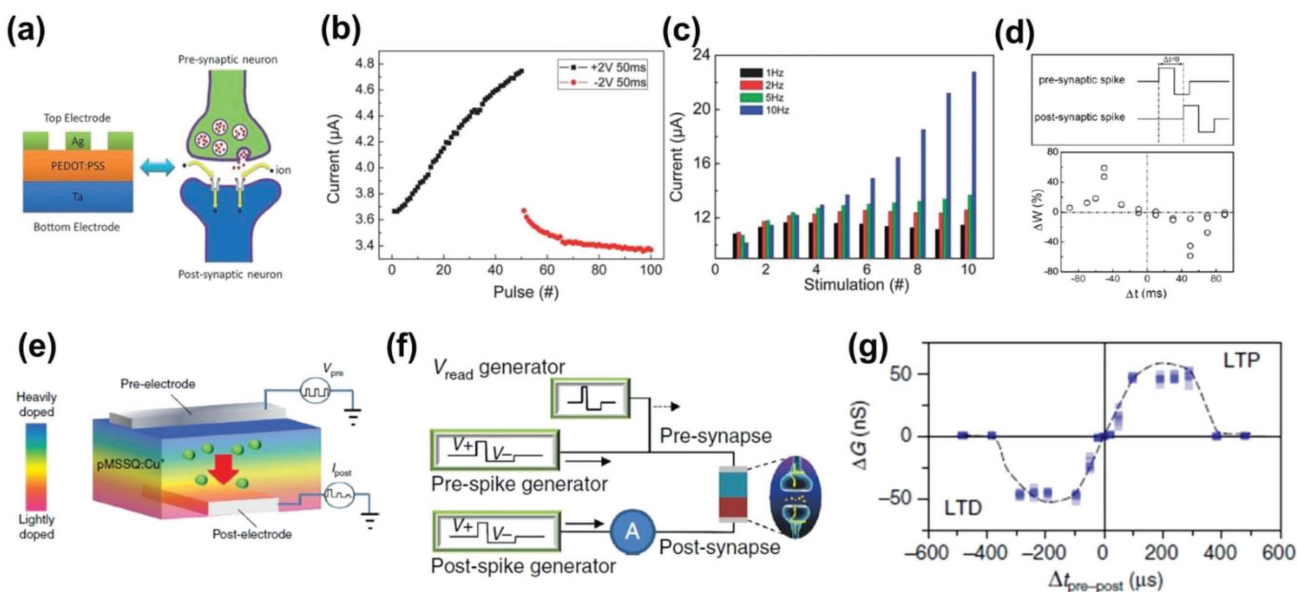


Figure 12. Device structures and synaptic behaviors of polymer-based artificial synapses. a) A device structure of Ag/PEDOT:PSS/Ta synapse correlated with biological synapse. b) Synaptic potentiation and depression behaviors by consecutive input pulses with the amplitude of 2 V and the duration of 50 ms. c) SRDP behaviors with the input pulse frequencies from 1 to 10 Hz. When the device frequency is the highest value of 10 Hz, the increasing rate is also higher than other conditions. d) STDP behaviors with the programmed presynaptic spike and postsynaptic spike. The synaptic weight is maximum when $\Delta t = \pm 50$ ms. Reproduced with permission.^[28] Copyright 2013, Royal Society of Chemistry. e) Schematic diagrams of a structure of Al/copper-ion-doped pMSSQ/Al synapse. If positive bias is applied to the top electrode, Cu ions are migrated toward the bottom electrode, which results in an increase of the barrier height and the decrease of the device conductance. f) The designed circuit for STDP measurement. The pMSSQ synapse is connected with spike generators which emulate neurons by inputting pre- and postsynaptic spikes to the electrodes. After the spike generation, a read pulse is generated to measure the device conductance. g) The STDP behaviors of programmed voltages by the designed circuit in (f). The LTP and LTD states are decided by the polarity of the synaptic weight, ΔG . Reproduced under the terms of the CC-BY Creative Commons Attribution 4.0 International License.^[29] Copyright 2017, Springer Nature.

low energy consumption of <10 pJ, which are extremely important for artificial synapses.

As a promising organic material, poly(methylsilsesquioxane) (pMSSQ) was also researched for artificial synapses owing to their 3D stacking capability, flexibility, and electrochemical stability by Wu et al. in 2017.^[29] They fabricated an Al/copper-ion-doped pMSSQ/Al structure, where the Cu ions have a concentration gradient that is higher in the vicinity of the top electrode, and lower near the bottom electrode as illustrated in Figure 12e. The pMSSQ layer works as a hole-injection material, and the doping amount of Cu determines the conductance of pMSSQ. The working mechanism of this device is based on the movement of Cu ions. They disclosed that Cu ions decrease the hole injection barrier by changing the highest occupied molecular orbital of Cu-pMSSQ to a lower binding energy level by UV photoemission spectroscopy. In other words, the large concentration of Cu ions is distributed to reduce the energy gap. When the positive bias is applied on the top electrode, many carriers could pass through the low barrier between the Al electrode and the Cu-pMSSQ layer, increasing the device conductance. The high concentration of Cu ions near the top electrode could lower the energy barrier. However, when the opposite bias is applied on the top electrode, the device conductance declines because the barriers between the Al bottom electrode and Cu-pMSSQ are higher due to the light Cu doping amount near the bottom electrode. In this case, the thermionic emission occurs rather than the carrier transport. They achieved gradual SET and RESET curve, LTP, LTD, and STDP (Figure 12g) properties, which proved that this device could be a promising candidate for artificial synapses. As shown in Figure 12f, the same programming input pulse of prespike and postspike are induced into the presynaptic electrode and the postsynaptic electrode, respectively. Because the spike direction between the prespike and postspike is opposite, the two spikes have a relatively reverse polarity. The pulse width of both spikes is 100 μ s; thus, when $\Delta t_{\text{pre-post}}$ is 200 μ s, their conductance change reaches the maximum value. The Δt ranging from -400 to 400 μ s achieves the LTP or LTD characteristics. In other words, if $|\Delta t| > 400 \mu\text{s}$, the presynaptic and postsynaptic cells are not connected to each other (Figure 12g).

Furthermore, Liu et al. in 2015^[30] reported an article about memristive and synaptic behaviors of ethyl viologen diperchlorate [EV(ClO₄)₂]/triphenylamine-containing polymer (BTPA-F) organic redox materials. They used Ta as the top electrode and Pt as the bottom electrode by creating a Ta/EV(ClO₄)₂/BTPA-F/Pt structure. In the BTPA-F layer, the redox reaction actively occurs with its closed ring and steric tightly packed TPA group. The EV(ClO₄)₂ group works as the counter-electrode and stabilizes the charged status. When the positive bias is applied to the top electrode, the BTPA-F group is oxidized by detaching the unpaired electrons from the N atoms. Then the ClO₄⁻ heads to the oxidized N atoms of the BTPA for neutralizing the total redox system. Meanwhile, the device conductance is effectively strengthened through the intrachain and the interchain hopping from the oxidized BTPA film. On the other hand, when the negative bias is applied to the top electrode, BTPA undergoes a reduction process; thus, the ClO₄⁻ anions return to their original form, resulting in low conduction of the device. They meet the gradual current change versus voltage avoiding an

abrupt change, which is a suitable property for application to electronic synapses. In addition, the potentiation and depression are emulated by this device with a pulse amplitude of ± 1 V, a duration of 10 ms, and an interval of 2 s. The potentiation and depression are observed by 50 repeated pulses. The SRDP behavior is also explored by differentiating the pulse frequency from 1 to 20 Hz. As expected, the case of 20 Hz pulses displays the largest current enhancing rate. The STDP property is clearly obtained following the asymmetric Hebbian learning rule with programmed pulses. Furthermore, the device could mimic the short-term memory (STM) and LTM behaviors. When continuous pulses are induced, the device undergoes the 1st learning process. After the decay process for 5 min, the device synaptic weight is reduced to an intermediate level. Then the 2nd learning is started not from the same initial value but from the same intermediate value. As the learning process is repeated, the device could translate STM to LTM.

4.2. Bioinspired Organics

Bio-inspired materials have excellent characteristics for application to resistive switching memories and artificial synapses. They have a simple fabrication process, biocompatibility, and flexibility. Generally, biopolymers refer to materials extracted by organisms in nature. Therefore, they are environment-friendly and do not require intricate synthesis and large amount of energy.^[31] Various novel biopolymers have been researched for memristors and artificial synapses such as lignin,^[31] chitosan,^[32–34] and proteins.^[35,36] In 2017, Park and Lee^[31] reported an article about flexible lignin-based synaptic devices. Lignin is a constituent of woods and considered as an arbitrarily connected polymer with complicated aromatic structures. Moreover, lignin has excellent characteristics, such as nontoxicity, high carbon concentration, and low cost, for application to artificial synapses. Owing to its high carbon content, it could be easily transformed to amorphous or graphite structures resulting in the change of electrical properties. Furthermore, because of its abundance in nature, it could be produced at low cost. They spin-coated lignin on ITO substrate and selected Au as the top electrode. Then they applied a DC voltage to the top electrode while carefully interrupting the abrupt resistance change. They obtained the *I*-*V* sweep curve of this device, which shows a gradual SET and RESET. In addition, various synaptic behaviors are observed by this device such as linear conductance change by continuous sweeps, and potentiation and depression profiles by 50 consecutive positive and negative pulses. The SRDP property is also monitored by applying different pulse interval times from 100 ms to 10 s. As predicted, when the pulse interval time is 100 ms, the current change rate becomes higher than in other conditions. They figured out the lignin thickness effect as well by adjusting the spin-coating speeds from 800 to 1200 rpm. The current level is slightly changed by the thickness effect. They also investigated the bending strength by a mechanical test. Furthermore, they explored the transition from STP to LTP by monitoring the synaptic weight decrease rate during the decay time. If the number of induced pulses is large enough, the synaptic weight is maintained at a certain level with respect to the LTP state. However,

if it does not exceed the threshold pulse number, it is reduced to almost 0% of synaptic weight. Moreover, the 2nd learning process is started from a higher basis by the 1st learning and it could reach the 100% synaptic weight level with less number of pulses than the 1st learning.

In 2016, Wu et al.^[36] researched an artificial synapse composed of natural chicken albumen coupled with three-terminal EDL transistors. Proteins have been actively researched as a promising candidate for substituting Si-based memristors, diodes, and transistors. Natural chicken albumen films, which consist of \approx 90% water and \approx 10% proteins contain high proton (H^+) conductivity; thus, they employed them as the electrolyte dielectric layer. They selected IZO as the top electrode and ITO as the bottom electrode. They extracted the chicken albumen from the white part of eggs and spin-coated it on the ITO substrate (Figure 13a). As shown in Figure 13a, the alteration of AFM images of ITO substrates is observed after the albumen is spin-coated. The RMS value is decreased from 2.709 to 1.068 nm, which means that the albumen film is smoother than the ITO substrate. The conducting mechanism of this device

is by proton migration, which resembles the interface type switching. When alternating current (AC) biases are inducted to the top electrode, it is observed by an extreme ultraviolet spectrometer that the interface is hydrogenated and the protons are transferred at a high frequency, while the EDL interface capacitance is formed at a low frequency. If a high voltage pulse is applied to the top electrode, more protons are transferred to the interface, and in turn, the device conductance is increased. By contrast, if the AC frequency is high, protons could not gain enough time to transfer to the interface; hence, the device conductance is reduced. From this device, important characteristics for artificial synapses are observed. First, the PPF is monitored with Δt of 20 ms in terms of EPSC, which is a basic representative of synaptic weight, as shown in Figure 13b. The second spike is larger than the first spike caused by the short interval time (20 ms) between the two spikes. Second, the SRDP profile is observed as shown in Figure 13c. The higher the frequency input pulses, the larger the EPSC increasing rate of this device. Third, they emulated the transition from STM to LTM by exploring the retention time difference between a large number

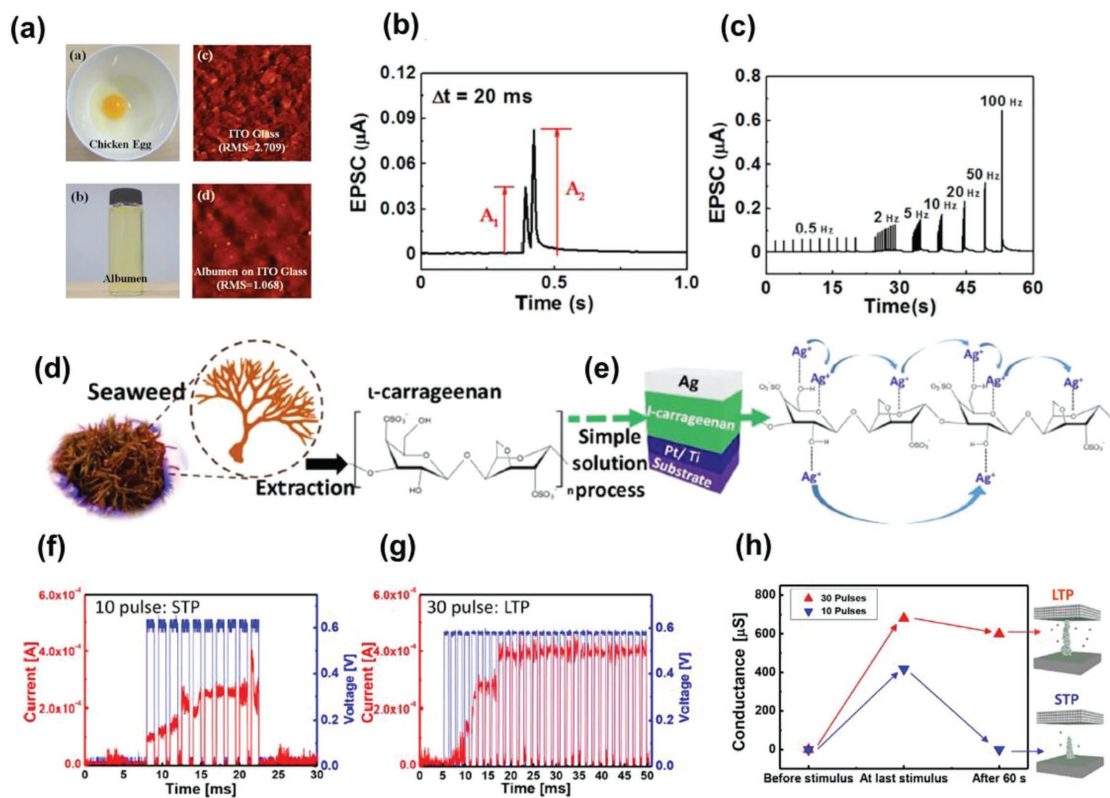


Figure 13. Device structures and synaptic behaviors of artificial synapses with bioinspired organic materials. a) Optical images of a chicken egg and albumen extracted by the white part of the egg. AFM images of an ITO glass substrate and albumen coated on the ITO substrate. b) Synaptic PPF behavior of an albumen-based artificial synapse. The second pulse is triggered by the first pulse. The time difference between the first and second spike is 20 ms. c) The EPSC behavior of the same device. If the input pulse frequency is higher, the post synaptic current becomes larger. The input pulse with high frequency of 100 Hz generated the largest post synaptic current. Reproduced under the terms of the CC-BY Creative Commons Attribution 4.0 International License.^[36] Copyright 2016, Springer Nature. d) The chemical structure and schematic illustration of *l*-carraageenan (*l*-car) extracted from seaweed. e) Schematic diagrams of migration of Ag cations through *l*-car exhibiting ECM in Ag/*l*-car/Pt device. f) A synaptic STP behavior achieved by ten consecutive input pulses of 0.6 V in a *l*-car-based artificial synapse. g) A synaptic LTP behavior achieved by 30 continuous input pulses of 0.6 V in the same device. h) The device conductance change in STP and LTP state. In STP state, the device conductance is decreased to the initial state after 60 s from the last stimulus. In LTP state, the conductance is remained in high level after 60 s from the last stimulus. Schematic illustrations show complete Ag CF in LTP state and rupture of the CF in STP state. Reproduced with permission.^[78] Copyright 2018, American Chemical Society.

of pulses ($N = 40$) and a small number of pulses ($N = 1$). If the amplitude or the number of pulses is large enough, more protons could migrate to the IZO channel layer, and in turn, the transition between STM to LTM is achieved.

Chitosan is one of the famous materials for resistive switching memories and artificial synapses. In 2015, Hosseini and Lee^[33] fabricated a structure of Mg/Ag doped chitosan/Mg, and achieved the 60th consecutive *I*-V sweep and a retention of 10^4 s. They also successfully proved its flexibility by 10^3 consecutive bending cycles with $\approx 10^2$ of on-off ratio. To form totally biocompatible and biodegradable devices, they suggested a biodegradable substrate such as rice paper and chitosan. They proved its biodegradability by displaying the totally dissolved Mg electrode and chitosan substrate by dropping deionized (DI) water on the device. In 2016, they suggested starch from potatoes and starch–chitosan composite materials as other promising candidates for memristor materials.^[34] Starch has remarkable advantages such as abundance, low cost, biodegradability, and biocompatibility. Starch from potatoes includes amylose, amylopectin, and bounded water molecules that cause ionic conductivity. The mixture of chitosan and starch is biodegradable owing to its high miscibility. Because of its biocompatibility, it could be applied for wearable electronic devices. They fabricated Au/starch/ITO and Au/starch–chitosan/ITO on a polyethylene terephthalate substrate, and obtained 10^4 s of retention current. The on-off current ratio of starch-based device is $\approx 10^3$ and that of starch–chitosan mixture is $\approx 10^2$. They also explored its flexibility by compressive and tensile bending tests, and showed successfully worked *I*-V sweeps with HRS and LRS. They revealed that the working mechanism is based on carbon-rich filaments (CRFs) by achieving the same resistive switching profiles by Ag top electrode. Because the resistive switching profiles are not affected by electrodes, CRF-based switching is possible by the local change in chitosan and chitosan–starch materials. They also discovered the *I*-V sweep difference between starch–chitosan and starch-based materials. For the starch–chitosan mixture materials, the density of carbon atoms is higher than that of starch-based materials. Hence, they postulated that the starch–chitosan composites can make multiple CRFs; thus, they show a gradual resistance change. In comparison, starch-based materials generate a single filament; therefore, they show an abrupt resistance change.

There is another novel artificial biosynapse introduced by Kim and Lee in 2018.^[78] They extracted *t*-carrageenan (*t*-car) from seaweed, which is known as a linear-sulfated polysaccharide biopolymer as shown in Figure 13d. They employed Ag dynamics for imitating the role of Ca²⁺ ions in biological synapses. The device structure is known as two-terminal Ag/*t*-car/Pt, where *t*-car works as a dielectric layer including C–O–C and C–O–H functional groups for interacting with metal ions. The resistive switching mechanism of this device is the redox reaction of Ag, which is known as ECM (Figure 13e). If a positive voltage is induced on the top electrode, the Ag electrode is dissolved and generates Ag⁺ cations. Then the Ag⁺ cations penetrate through the *t*-car layer, head to the Pt bottom electrode, and undergo a reduction process near the interface between the bottom electrode and *t*-car layer as growing a Ag CF. As a promising candidate for artificial synapses, an *t*-car device successfully obtained SRDP behaviors. As shown in Figure 13f,g,

the repetitive number of pulses determines the device characteristics, whether it is STP or LTP. When they applied ten consecutive pulses, the current is abruptly decreased after the pulses are removed. However, when they induced 30 continuous pulses, the current is maintained after the pulses are removed. The conductance values before stimulus, at the last stimulus, and after 60 s indicate that the 30 pulses meet the LTP state by creating a wide CF, while 10 pulses achieve an STP state by obtaining a weak and narrow CF as visually illustrated in Figure 13h. This phenomenon could represent the transition from STM to LTM. They proved the ability of STM and LTM emulation by a distinct simulation implemented by inputting two letters of "P" and "T" to the *t*-car device. They inputted "P" 10 times and "T" 30 times. After 60 s, they observed that only "T" is maintained. They also revealed that the thickness of *t*-car has an effect on the resistive switching behavior by changing the *t*-car spin-coating speed from 1000 to 2600 rpm. As the thickness becomes thinner, the activation voltage reduces.

5. 2D Materials

5.1. Graphene

Graphene was first described by Novoselov et al. in 2004^[37] as a single-layer 2D material and has been actively examined for various applications such as FETs, sensors, and transparent conductive films.^[38] Graphene is composed of a 2D array of carbon, which appears with a honeycomb lattice.^[39] Graphene is one of the highly researched materials for bioinspired electronic devices owing to its excellent properties of low cost, tunability, nontoxicity, flexibility, and biocompatibility.^[40,106] For artificial synapses, graphene has been researched as a bottom electrode,^[40,107] electrolyte dielectric layer,^[108–110] and ion-blocking layer.^[41] In 2017, Tian et al.^[40] fabricated Al/AlO_x/graphene three-terminal transistors and observed their synaptic behaviors. In this structure, the bottom electrode is a bilayer graphene, which acts as the channel, and the oxygen vacancies in AlO_x layer work as trapping centers. In order to achieve a gradual analog-type resistance change, they divided the test Modes as I and II. In Mode I, the device shows an abrupt resistance change due to the tunneling gap between the oxygen vacancy filament and Al/AlO_x interface. The tunneling gap is changed by an applied electric field and causes abrupt changes. On the other hand, in Mode II, the oxygen vacancy filament is not created. Instead of forming a filament, the oxygen vacancies are gathered at the AlO_x/graphene interface called carrier trapping sites (Figure 14a). The main difference between Mode I and II is the way of operating the device. In Mode I, the back gate, source, and drain are all grounded, and the postsynaptic current is gathered from the leakage current of the gate. However, in Mode II, the back gate and source are grounded, but the drain is biased. The postsynaptic current is gathered from the drain current. From Mode I, gradual SET and RESET profiles are observed in the positive and negative DC sweeps, but during repetitive pulse measurements, the current level is abruptly increased due to the change in the tunneling gap. A gradual change in RESET is obtained; hence, Mode I shows depression-only behavior. To achieve gradual potentiation and depression

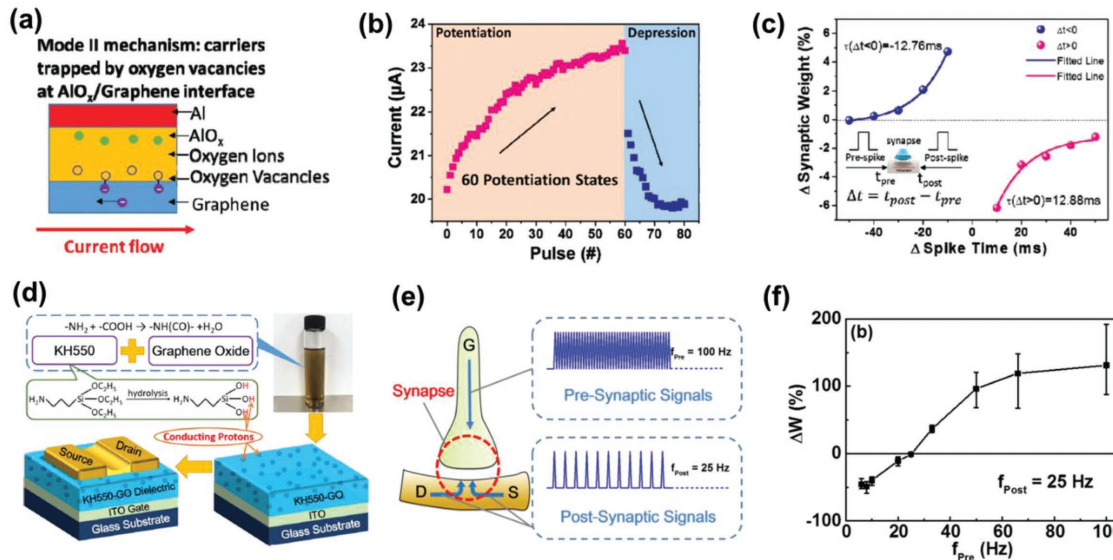


Figure 14. Device structures and synaptic behaviors of graphene-based electronic synapses. a) A schematic of Al/AlO_x/graphene structure in FET mode. Instead of forming a filament, the oxygen vacancies are trapped in the AlO_x/graphene interface generating gradual conductance increment. b) Synaptic potentiation and depression behaviors of the graphene bottom electrode device. c) A STDP behavior which follows asymmetric anti-Hebbian learning rule. Reproduced with permission.^[40] Copyright 2017, RSC Publishing. d) Schematics of KH550-GO based three-terminal artificial synapse and the chemical structure of KH550-GO mixture. e) A schematic diagram of presynaptic signals and postsynaptic pulses in the three-terminal KH550-GO based device. f) A SRDP behavior from the pre- and postsynaptic pulses illustrated in (e). Reproduced with permission.^[110] Copyright 2016, American Chemical Society.

behaviors, they tried to develop Mode II, where the charge-trapping center in AlO_x is linearly formed by applied pulses. Therefore, the electrons in graphene could linearly be trapped and untrapped from the trapping center. It arouses linear potentiation and depression behaviors as illustrated in Figure 14b. If a positive bias is applied, the oxygen ions in graphene are drifted toward the Al electrode while oxygen vacancies remain at the bottom of the AlO_x layer. Hence, the induced bias causes more electrons that flow in the channel to be trapped by the oxygen vacancies. Therefore, there is less electron flow through the channel causing depression. On the other hand, if a negative bias is applied, the detrapping of electrons from AlO_x leads to an increase in electrons in the channel, achieving potentiation reactions. Moreover, the STDP behavior, which corresponds to the asymmetric anti-Hebbian learning rule, is observed in Mode II as shown in Figure 14c.

Graphene has also been researched as a dielectric layer for memristors and artificial synapses. In 2016, Yang et al.^[110] fabricated three-terminal bioinspired devices with IZO thin film transistors. As shown in Figure 14d, graphene oxide (GO) could be simply altered by 3-triethoxysilylpropylamine (KH550) because of the condensation process between $-\text{NH}_2$ groups of KH550 and $-\text{COOH}$ groups of GO. Because KH550-GO has plenty of $-\text{SiOC}_2\text{H}_5$ and it is able to be hydrolyzed to $-\text{SiOH}$, it has high proton conductivity. Therefore, they employed KH550-GO as gate materials. The device structure is composed of IZO/KH550-GO/ITO, where the IZO channel is self-assembled to connect the IZO source and drain as illustrated in Figure 14d. They monitored the postsynaptic current from the channel layer, and regarded the voltage applied on the ITO as the pre-synaptic spike. In this device, the ITO bottom electrode emulates a preneuron; the IZO channel, source, and drain mimic a

postneuron, and the current flow in the IZO channel imitates the synaptic weight as described in Figure 14e. They successfully obtained SRDP behaviors as described in Figure 14f. When the frequency of postsynaptic pulses (f_{post}) is fixed as 25 Hz, the percentage (%) of synaptic weight change (Δw) is determined by the frequency of presynaptic pulses (f_{pre}). As shown in Figure 14f, Δw is proportional to f_{pre} ; therefore, f_{pre} , which exceeds the threshold frequency, derives the imitation of LTM in this device.

In 2016, Lee et al.^[41] tried to control the ion migration in order to optimize the memristive performance by fabricating a two-terminal Ta/graphene/Ta₂O₅ device, where the graphene works as an ion blocking layer. They developed the idea of employing graphene as an ion blocking layer from articles that explain the excellent impermeability of graphene. In 2008, Bunch et al.^[111] examined the gas impermeability of a monolayer graphene. In addition, in 2010, Garaj et al.^[112] demonstrated that only two atomic layers of graphene could work as an excellent blocker between two ionic solutions. They exploited the nanopores in graphene for the oxygen ion migration from Ta₂O₅ layer to a Ta top electrode. Conventional memristors with Ta/Ta₂O₅ have caused problems in the RESET process because the uncontrollable filament becomes wider, inhibiting the RESET process and causing it to be stuck in LRS. Because graphene has an excellent impermeability, the oxygen ions could migrate only through the nanopores. In other words, the CF formation occurs only at the region of the nanopores, and the filament size is also decided by the size of nanopores. For the characterization of nanopores, it was reported by O'Hern et al. that the nanopores with ≈ 10 nm size could be created by a chemical vapor deposition process.^[113] By inserting this graphene with nanopores between a Ta and Ta₂O₅ layer, they observed that the

current levels of SET and RESET are reduced, and the device reliability is higher compared to conventional Ta/Ta₂O₅ memristors. To produce the desired nanopores, they created a multi-layer graphene (MLG) for blocking the random nanopores of each layer. They postulated that the nanopores at each layer are randomly created; thus, the nanopores are blocked when they pass through each impermeable graphene layer. Then they created artificial nanopores with sizes of 25–400 nm by e-beam lithography and oxygen plasma etching. By this MLG engineering, they could create a single nanopore for each device with different sizes. Then they demonstrated that the device conductance is proportional to the size of nanopores. The LRS and HRS current graph shows that when the hole diameter increases, the LRS and HRS current also increases. The *I*–V sweeps of the device also show that the current level is proportional to the hole diameters. Furthermore, they discovered that the forming voltage has less variation than that of the Ta/G/Ta₂O₅ device. They proved the ion blocking effect of graphene by annealing both Ta/G/Ta₂O₅ and Ta/Ta₂O₅ devices. Both devices show a decrease in resistance because of the increasing

ion diffusion rate owing to the annealing effect. However, Ta/G/Ta₂O₅ devices obtain a mild decrease in their resistance while Ta/Ta₂O₅ shows a high decreasing rate. Hence, the ion diffusion rate is controlled by the ion blocking layer, which is graphene. Although they did not examine the synaptic behaviors of this device, the ion blocking engineering with graphene has remarkable possibilities of being applied to bioinspired electronics owing to its conductance control ability.

As one of the promising materials for artificial synapses, graphene could be transformed to graphene quantum dots (GQDs) and applied for electronic synapses. In 2017, Choi et al.^[114] fabricated an Al/PEDOT:PSS:GQDs/ITO/glass device as shown in Figure 15a,b. GQDs have excellent characteristics such as excitation-dependent photoluminescence, energy level variability, and charge-storage ability. They could save charges at charge trapping sites, where the migration properties of polymer nanocomposites included in GQDs are affected. The authors fabricated a PEDOT:PSS:GQD layer by mixing a PEDOT:PSS solution and a GQD suspension in DI water and spin-coating the mixed solution on the ITO substrate. The GQD concentrations

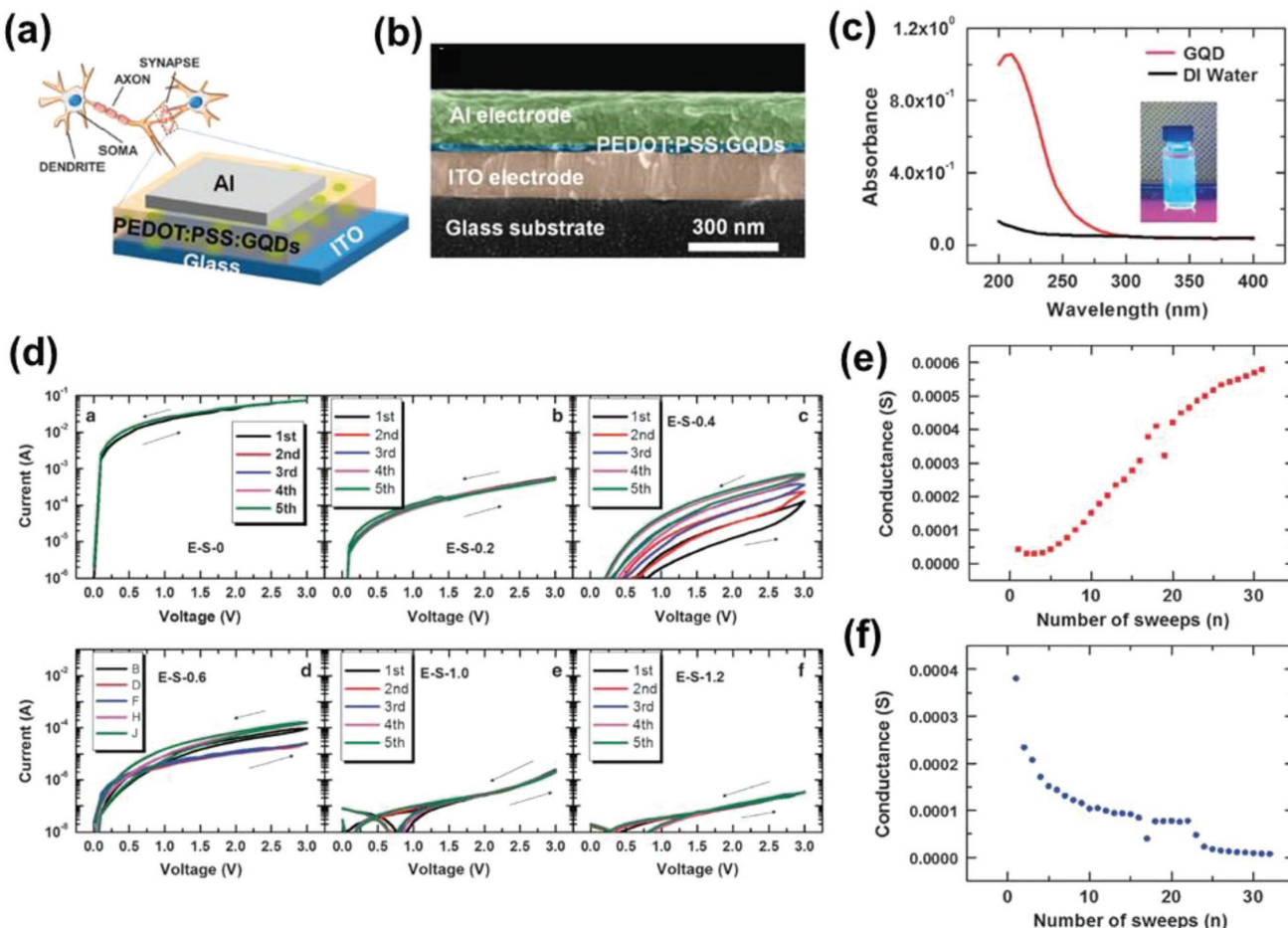


Figure 15. A device structure and synaptic behaviors of PEDOT:PSS:GQDs-based artificial synapse. a) Schematic diagram of Al/PEDOT:PSS:GQDs/ITO electronic synapse. b) Cross-sectional SEM image of the same device. c) UV-vis spectra of the GQD compared with DI water. GQDs under 365 nm illumination achieve bright blue emission. d) *I*–V sweeps according to the solution amount of GQDs with 0, 0.2, 0.4, 0.6, 1, and 1.2 mL. When the GQDs amount is 0.4 mL, the gradual increase of current clearly appears without overlapping. e) A synaptic potentiation behavior by positive voltage sweeps. f) A synaptic depression behavior by negative voltage sweeps. Reproduced under the terms of the CC-BY Creative Commons Attribution 4.0 International License.^[114] Copyright 2017, Springer Nature.

are varied by the solution amounts of GQD at 0, 0.2, 0.4, 0.6, 1, and 1.2 mL. As shown in Figure 15c, the GQD in DI water appears in bright blue emission under a 365 nm illumination. The *I*-*V* sweep differences due to the concentration effect of GQDs are illustrated in Figure 15d. Because PEDOT:PSS is a conducting polymer, the pure PEDOT:PSS shows the highest current level. By increasing the concentration of GQDs, the device current level decreases. As shown in Figure 15d, the GQD concentration of 0.4 mL (E-S-0.4) showed the best gradual increase and decrease in current, which satisfies the requirements of artificial synapses. Moreover, the GQD concentration of 0.6 mL (E-S-0.6) shows a little overlap between each sweep, showing a slight probability for artificial synapses. They also demonstrated the conductance versus number of sweeps as shown in Figure 15e,f. When the sweep is induced as 0–3–0 V dual sweep, the conductance is gradually increased, changing the device state from HRS to LRS by repetitive positive sweeps (Figure 15e). When the negative dual sweep of 0 to –3 to 0 V is induced, the device conductance is gradually decreased from LRS to HRS (Figure 15f). This emulates the potentiation and depression in biological synapses. They also discovered the carrier migration mechanism of this device by fitting the *I*-*V* curves, and obtained the α value of I - V^α . When the voltage is below 0.5 and –0.5 V, respectively, it is Ohmic-conduction dominant owing to the linearity of *I*-*V* fittings. However, if the induced voltage is greater than 0.5 V, the α value is 2.97; thus, the conduction is space-charge-limited-current (SCLC) dominant. Furthermore, when the induced voltage is above –0.5 V, the α value changes from 2.59 to 4.73, and the conduction mechanism is SCLC as well. Based on the understanding of the conduction mechanism and discovering the optimized GQD concentration, they demonstrated a possible electronic synapse,

which could imitate the potentiation and depression behaviors of biological synapses. It is required to achieve more synaptic behaviors such as STDP and SRDP from further studies.

5.2. Molybdenum Disulfide

Molybdenum disulfide (MoS_2) has been researched as one of the 2D materials that show superior scalability compared to 3D materials. Because MoS_2 is a type of semiconductor that has a band gap from 1.2 eV of the bulk to 1.8 eV of monolayers, it has been considered to be able to substitute a highly examined 2D graphene, which has a zero band gap.^[42] In 2014, Bessonov et al.^[43] fabricated a $\text{MoO}_x/\text{MoS}_2$ ($x < 3$) sandwiched between a Ag bottom and top electrodes, which are printed (Figure 16a). Because there is a limitation in the oxygen diffusion of MoS_2 , the oxidation thickness of MoS_2 is limited within ≈ 3 nm. The oxidation process could be explained by Equation (5)



It is obvious that the ion vacancy concentration of its surface is less than that of the bulk; therefore, the oxygen concentration gradient is naturally generated according to the depth. Hence, the charge transfer is generated by charge trapping and detrapping in the vicinity of the Ag/ MoO_x interface. The two-terminal Ag/ $\text{MoO}_x/\text{MoS}_2/\text{Ag}$ device shows an ideal *I*-*V* sweep with the transition from HRS to LRS as shown in Figure 16b. They also discovered that the top electrode material critically influences the *I*-*V* sweeps because the top electrode is directly attached to the MoO_x layer. The *I*-*V* sweep variation with different top electrodes are shown in Figure 16c with Ni, Ag, MoS_2 , and AgNW.

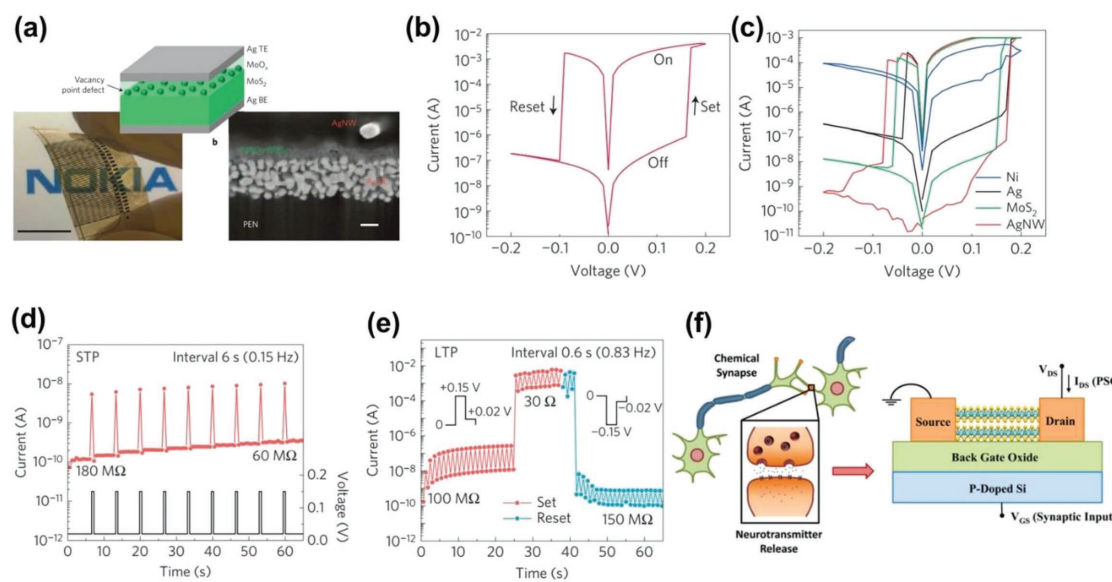


Figure 16. Device structures and synaptic behaviors of MoS_2 -based artificial synapses. a) A schematic diagram and cross-sectional SEM image of Ag/ $\text{MoO}_x/\text{MoS}_2/\text{Ag}$ device. An optical image of transparent $\text{MoO}_x/\text{MoS}_2$ -based device. b) *I*-*V* sweep with SET and RESET profile. c) *I*-*V* sweeps of different top electrode materials. The compliance current is 10^{-3} A. d) A STP behavior by input pulses with 0.15 V for 0.6 s and the pulse interval with 6 s. e) A LTP behavior by input pulses with 0.15 V for 0.6 s and the pulse interval with 0.6 s. Reproduced with permission.^[43] Copyright 2014, Springer Nature. f) Schematic illustrations of a three-terminal back-gated MoS_2 FET which imitates neurotransmitters dynamics in biological synapses. Reproduced with permission.^[115] Copyright 2017, American Chemical Society.

(AgNW), and MoS₂. They also revealed that the device structure with AgNW/MoO_x/MoS₂ emulates the STP behaviors with a long pulse interval time of 6 s (Figure 16d), and LTP behaviors with a short interval time of 0.6 s (Figure 16e). Overall, it is proved that this device could emulate the SRDP of biological synapses. A major problem of this device is that the LTP behavior contains abrupt changes at ≈ 25 and 40 s. These abrupt changes should be overcome to produce reliable electronic synapses.

One of the noticeable progresses of MoS₂ memristors is a gate tunable possibility by its electroformed GBs by an applied bias to a single-layer MoS₂. In 2015, Sangwan et al.^[44] found that sulfur vacancies are accumulated near the GB, changing the resistance state in different profiles according to the type of GB, i.e., either intersecting or bridging. They discovered that in the intersecting GB case, which is parallel to the electrodes, the gate voltage could be changed from 0 to 40 V; thus, the SET voltage could be changed from 3.5 to 3.8 V. Moreover, to achieve more functions of biological synapses by the GB dynamics, Arnold et al. in 2017^[115] released an article about a three-terminal back-gated MoS₂ FET as shown in Figure 16f. The MoS₂ layer connects the source and drain and acts as a channel. They focused on emulating the release dynamics of neurotransmitters by MoS₂ FET. The gate voltage pulses of this device emulate a presynaptic spike, and the source to the drain current mimics the postsynaptic current. The postsynaptic current represents the charge transport amount through the gate material, which is MoS₂. Furthermore, the transported charges emulate neurotransmitters in biological synapses. The charge transport mechanism is explained as interface charge trapping

and detrapping at the MoS₂ surface. They differentiate the characteristics of gate voltage pulses such as their amplitude, frequency, and polarity, which correspond to the characteristics of prespikes in biological synapses. From this concept, they observed that varying the back-gate voltages and drain biases causes changes in the source to drain current (ΔI_{DS}). As a result, they demonstrated the excitatory and inhibitory response of EPSC from ΔI_{DS} by positive and negative gate voltage pulses ranging from 10 to 60 V and -10 to -60 V, respectively. The positive gate pulses generate inhibitory responses, and the negative gate pulses create excitatory responses. They also collected the profiles of LTP from the off state operation of the MoS₂ FET. Recently, Sangwan et al.^[116] in 2018 improved the three-terminal MoS₂ FET concept to multiterminal memtransistors with polycrystalline MoS₂. By producing multiterminal devices, it is possible to modulate each terminal and perform a delicate tuning of its electrical properties. Multiterminal memtransistors could also possess heterosynaptic behaviors by gate electrode, where the switching amount could be varied. They also found the potentiation, depression, and STDP behaviors from this device.

Furthermore, in 2017, Jiang et al.^[42] tried to achieve synaptic behaviors such as EPSC and PPF by a three-terminal poly(vinyl alcohol) (PVA)-coupled MoS₂ transistor to remove the requirement of water and oxygen molecules for oxidation of MoS₂ to MoO_x. As shown in Figure 17a, a 2D MoS₂ coupled with PVA connects a source and drain to work as a channel. The top view of the optical image also indicates that the two gold electrodes, the source and drain, are connected by MoS₂ (Figure 17b). By employing a proton conducting PVA, which has a leakage

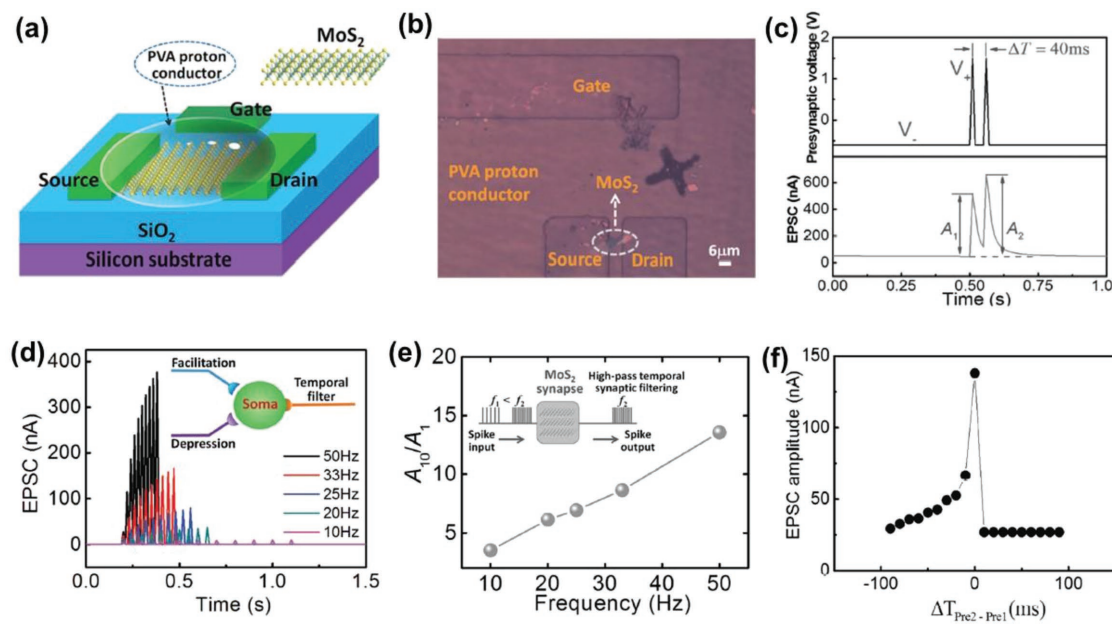


Figure 17. Device structure and synaptic behaviors of a three-terminal MoS₂ channel synaptic transistor. a) A schematic of three-terminal PVA-coupled MoS₂ artificial synapse. b) A top view of an optical image which indicates that MoS₂ connects the gold source and drain electrodes. c) Synaptic PPF with the time difference of 40 ms. The second pulse is triggered by the first pulse. d) A SRDP behavior according to the input pulse frequencies. When the pulse frequency is 50 Hz, it shows the largest increasing rate of EPSC. e) The ratio of EPSC between the tenth pulse (A_{10}) and the first pulse (A_1), which shows the increasing pulse frequency results in the increment of the EPSC ratio, A_{10}/A_1 . f) A STDP behavior with two spikes. The spike 2 emulates a prespike and the spike 1 mimics a postspike. According to the time difference between the two spikes, EPSC is determined with positive or negative values. Reproduced with permission.^[42] Copyright 2017, Wiley-VCH.

current for ion migration depending on the external voltage amplitude, the proton could move toward the MoS₂ channel layer by increasing the channel conductance. Owing to the sufficiently charged protons in the PVA layer, it is expected that the device could obtain synaptic behaviors easily. In this device, the gate emulates the presynaptic spike terminal, and the MoS₂ channel mimics the path where the postsynaptic current could be measured. In this device, they successfully obtained PPF with a pulse interval of 40 ms (Figure 17c). The presynaptic pulse changes the conductance of the MoS₂ channel layer, and it is maintained until the postsynaptic second pulse is induced. Hence, the second EPSC is higher than the first one, which is called PPF. The SRDP behavior is also achieved in this device as shown in Figure 17d. When the frequency is high enough such as 50 Hz, a huge potentiation is achieved while a low frequency of 25 Hz results in a slight increase in EPSC, and that of 10 Hz does not show any changes in EPSC. In addition, they demonstrated the ratio between the EPSCs of the tenth (A₁₀) and the first (A₁) as illustrated in Figure 17e. Similar to Figure 17d, the increasing ratio of EPSC between A₁₀ and A₁ is proportional to the pulse frequency, which resembles the SRDP behavior of biological synapses. To demonstrate STDP-like behaviors, they postulated that spike 2 is a prespike and spike 1 is a postspike. If Δt_{spike2–spike1} < 0, the prespike precedes the postspike; thus, the EPSC amplitude is higher. By contrast, if Δt_{spike2–spike1} > 0, the prespike is induced after the postspike; hence, the accumulated protons at the interface between MoS₂ and PVA layer are drifted back to their initial position and the amplitude of EPSC becomes the same as that triggered by spike 1 (Figure 17f).

6. Halide Perovskites

6.1. 3D Halide Perovskites

Halide perovskites have been highlighted owing to their significant advantages such as rapid ion migration,^[117] solution process availability,^[2,76,77,118] tunable band gap,^[3,119] and long charge-carrier diffusion length.^[120] Because of these advantages, halide perovskites have been considered as promising candidate materials for resistive switching memories. In the past few years, researchers have actively demonstrated the properties of halide perovskite memristors with their *I*-V sweep, endurance, and retention.^[76,118,121] In 2016, Yoo et al.^[46] successfully fabricated a Ag/CH₃NH₃PbI_(3-x)Cl_x/FTO structure (Figure 18a) and demonstrated its properties as a resistive switching memory and artificial synapses. They discovered the *I*-V sweep profiles of this device by sweeping voltages with 0 V → 3 V → -3 V → 0 V. They figured that the mechanism of this device is ECM by Ag filament, where positive biases generate a Ag CF by Ag⁺ cation migration and reduction near the FTO electrode, while negative biases lead to the rupture of the Ag CF by Joule heating. As a result, positive biases change the device state to LRS, and negative biases convert the device state to HRS. From the fitting data, they demonstrated that the charge migration is caused by a trap-controlled SCLC process including an Ohmic conduction area (*I* ∝ *V*), a Child's law area (*I* ∝ *V*²), and an abruptly increased area. Moreover, they discovered the light effect of CH₃NH₃PbI_(3-x)Cl_x with simulated

sunlight (100 mW cm⁻²). The voltages of SET and RESET are reduced from ≈±1.5 to ±0.3 V because the excessive charge carriers are generated under the simulated light. Furthermore, they observed gradual SET and RESET profiles by consecutive voltage sweeps of 0 → +0.5 → 0 V and 0 → -0.5 → 0 V as shown in Figure 18b,c. A digital switching, which appears as HRS or LRS, occurs by a complete Ag filament that connects a top electrode and a bottom electrode. By contrast, an analog switching, which indicates gradual changes, is generated by an incomplete Ag filament. In this case, when the sweep voltage of 0 → +0.5 is induced, Ag atoms in the top electrode could be gradually migrated to the FTO bottom electrode from the interface between the Ag electrode and the CH₃NH₃PbI_(3-x)Cl_x layer. Then, the effective gap between the top and bottom electrode could be reduced, which causes the increase in its current level. Because the accumulated Ag atoms are not dissolved until a negative bias is applied, the Ag filament maintains its previous form when the voltage is changed from +0.5 to 0 V. As a result, the consecutive sweeps of 0 → +0.5 → 0 V gradually decrease the effective gap between the two electrodes and increase the lateral size of the Ag filament, which causes a gradual increase in its current level. The *I*-V sweeps in Figure 18b,c show a typical analog resistive switching. As shown in Figure 18d, potentiation and depression, which mimic biological synapses, are achieved by repeated pulse type biases of +0.5 and -0.5 V, respectively, with a read pulse of +0.2 V. When 10 positive pulses of +0.5 V are repeatedly induced, the current level is linearly increased from ≈0.5 to 0.75 μA, which emulates the synaptic behavior of potentiation. The following 10 pulses of -0.5 V lead to a linear decrease in the current level from ≈0.7 to 0.5 μA, which mimics depression. This device shows three repetitive sets of potentiation and depression.

In 2016, Xu et al.^[5] also reported synaptic behaviors of a two terminal Al/CH₃NH₃PbBr₃/BCCP device as illustrated in Figure 18e. BCCP is composed of PEDOT:PSS, a perfluorinated ionomer, and tetrafluoroethylene-perfluoro-3,6-dioxa-4-methyl-7-octenesulfonic acid copolymer (PFI). As shown in Figure 18f, by applying step voltages from -2 to -6 V consecutively, the current levels are gradually increased. Moreover, when positive step voltages of 2 and 3 V are continuously applied, the device current level gradually decreased. This analog switching imitates the potentiation and depression of biological synapses. In this device, pulse type voltages applied on the top electrode imitate the prespikes induced on the preneuron. The measurement of EPSC at the BCCP bottom electrode, which indicates abrupt changes in the current level in CH₃NH₃PbBr₃ layer, corresponds to the synaptic weight in biological synapses. They successfully obtained an EPSC similar to that in biological synapses by applying electrical pulses on the Al top electrode. As explained above, STP is a transient modification of the synaptic strength, which rapidly reverts to the original state unless the synaptic stimuli are repeated. PPF is one of the STPs when increasing the current level temporarily by the second input pulse, which closely follows the first input pulse. In a biological synapse, the synaptic strength is increased by the concentration of Ca²⁺ ions in the presynaptic membrane, because Ca²⁺ ions trigger the emission of neurotransmitters. Similarly, synaptic weights in electronic synapses are increased if a pair of continuous pulses is induced. The change rate of

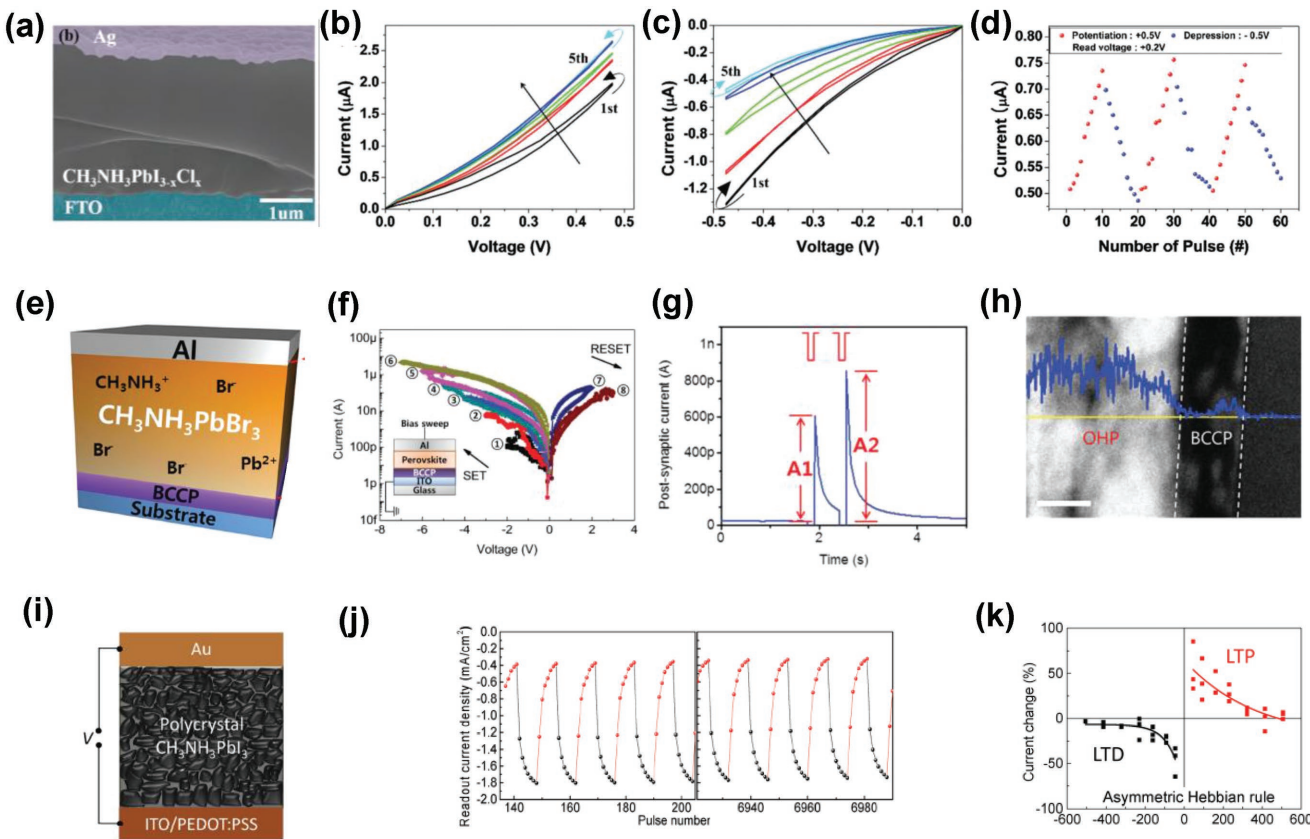


Figure 18. Device structures and synaptic behaviors of halide-perovskite-based artificial synapses. a) Cross-sectional SEM image of the $\text{CH}_3\text{NH}_3\text{PbI}_{3-x}\text{Cl}_x$ -based artificial synapse with a Ag top electrode and FTO bottom electrode. b) I - V sweeps with continuous $0 \rightarrow 0.5 \rightarrow 0$ V sweeping which achieve gradual increase and show a potentiation profile. c) I - V sweeps of depression profile with repetitive $0 \rightarrow -0.5 \rightarrow 0$ V which shows gradual decrease. d) Synaptic potentiation and depression profiles from pulse type biases. The potentiation is achieved from ten pulses of 0.5 V, and the depression is obtained from ten pulses of -0.5 V. Repeated three sets of potentiation and depression are achieved. Reproduced with permission.^[46] Copyright 2016, Royal Society of Chemistry. e) A schematic diagram of Al/ $\text{CH}_3\text{NH}_3\text{PbBr}_3$ /BCCP artificial synapse. f) I - V sweeps which contain gradual SET and RESET. g) Synaptic PPF by consecutive two pulses. The second pulse is triggered by the first pulse. h) Cross-sectional TEM image and Br EDS profile of $\text{CH}_3\text{NH}_3\text{PbBr}_3$ /BCCP interface. After inducing enough series of input pulses to generate LTP, the Br element peak is observed in the BCCP layer. It indicates the working mechanism is based on the Br^- ions movement. Reproduced with permission.^[5] Copyright 2016, Wiley-VCH. i) A schematic diagram of two-terminal Au/ $\text{CH}_3\text{NH}_3\text{PbI}_3$ /PEDOT:PSS/ITO synapse. j) Synaptic potentiation and depression profiles with -2.0 V, $+2.0$ V, and read pulse of -0.75 V. k) A STDP behavior which follows asymmetric Hebbian learning rule and contains LTP and LTD state. Reproduced with permission.^[45] Copyright 2016, Wiley-VCH.

synaptic weight is determined by the time interval between two spikes and the amplitude of input pulses. As shown in Figure 18g, PPF is successfully obtained from this device, which shows a larger EPSC at the second pulse affected by the first pulse. Moreover, the effect of pulse width is also obtained by applying input pulses from 70 to 1050 ms. As the pulse width is increased, the EPSC also rises, which corresponds to the SRDP in biological synapses. The STDP behavior of this device is also observed as following the asymmetric Hebbian learning rule. Moreover, the minimal energy consumption of this device is revealed to be ≈ 20 fJ, which is calculated by multiplying A (the amplitude of the pulse), I (postsynaptic current), and t (pulse duration time). In this device, the working mechanism is the ion vacancy defect because the applied pulses lead to migration of ions. When the pulse amplitude and number are not enough, some ions migrate to a small distance and rapidly return to the original positions, which is analogous to STP. On the other hand, when a high amplitude or many pulses are

induced, the ions migrate to a long distance and are trapped to the $\text{CH}_3\text{NH}_3\text{PbBr}_3$ /BCCP interface. It is observed that some ions even penetrate into the BCCP layer. After the pulses are removed, some ions are still trapped in the BCCP layer. Hence, the increased current level is maintained for a long time, which is analogous to LTP in biological synapses. The activation energy (E_a) of Br^- (0.2 eV) is the lowest among other ions; thus, Br^- is the dominant migration ion determining the device conductance. The article is important because it shows the EDS profile and proves its working mechanism by showing the Br^- peak at the BCCP layer as shown in Figure 18h. In halide perovskites, the E_a of halide ions is generally the lowest among other ions; thus, they dominantly contribute to the increase and decrease in device conductance.^[122]

In 2016, Xiao and Huang^[45] also reported the properties of a Au/ $\text{CH}_3\text{NH}_3\text{PbI}_3$ /PEDOT:PSS/ITO two-terminal synaptic device as illustrated in Figure 18i. Similar to the above halide perovskites, the working mechanism of this device is also by the

I^- ion or CH_3NH_3^+ interstitial ion migration. When positive polarity pulses are induced, V_i^- or MA_i^- moves to the Au side or V_{MA} or V_{Pb} migrates to the PEDOT:PSS side. Therefore, the device is switched to the p-i-n direction. On the other hand, when negative polarity pulses are applied, the device is changed to p-i-n. If the density of GB is larger, the ion migration speed becomes higher through the GBs owing to their open structure. Hence, obtaining smaller grains in halide perovskite films is important to facilitate the ion migration for resistive switching memories and synaptic device applications. Through these ion migrations according to the pulse polarity, the potentiation and depression behaviors are achieved as shown in Figure 18j. The STDP, SRDP, LTP, and STP behaviors are also obtained from this device. As shown in Figure 18k, the STDP, which follows the asymmetric Hebbian learning rule is obtained, and the behaviors of the asymmetric anti-Hebbian, symmetric Hebbian, and symmetric anti-Hebbian learning rules are also achieved according to different programmed pulses.

Halide perovskites show remarkable on-off ratios, high switching speed, low operation voltages, and synaptic behaviors, but their air stability still needs to be improved for their applications to memristors and artificial synapses.

6.2. 2D Halide Perovskites

Halide perovskites with 2D layers have a composition of $(L)_2(\text{SMX}_3)_{n+1}\text{MX}_4$. The L and S indicate the long-chain and short-chain of organic cations, and M and X are analogous to a divalent metal and a halide ion. 2D halide perovskites have been highlighted owing to their low operating current and wide band gaps. Recently, Kumar et al.^[123] and Tian et al.^[124] reported 2D perovskite memristors and artificial synapses. In 2017, Tian et al.^[124] showed that a 2D Ruddlesden–Popper phase $(\text{PEA})_2\text{PbBr}_4$ with a graphene top electrode and an Au bottom

electrode is available for memristors and artificial synapses with low operating current. As shown in Figure 19a, $(\text{PEA})_2\text{PbBr}_4$ single crystals are synthesized by modified antisolvent vapor-assisted process, and appear as exfoliated layers. Because the single crystal $(\text{PEA})_2\text{PbBr}_4$ has no GBs and pin holes, its leakage current is extremely low. Moreover, $(\text{PEA})_2\text{PbBr}_4$ has a wide band gap of ≈ 2.9 eV, which is an important characteristic because other 2D semiconductor materials are known as exhibiting relatively narrow band gaps. The narrow band gap generates an excellent path to examine the ion transport in the perovskite layer owing to its low carrier density. Consequently, ultralow SET and RESET currents are obtained as 10 and 3 pA, respectively. The endurance of 100 cycles with an on-off ratio of ≈ 10 is also achieved, and the retention time is determined as 10^3 s. Moreover, through Monte Carlo simulation, it is proved that Br^- ion migration creates a Br^- ion vacancy filament, which contributes to the increase and decrease in device conductance. As a promising artificial synapse, this device obtained a gradual STP by applying six input pulses as shown in Figure 19b. Furthermore, by the second set of six input pulses, the transition from STP to LTP is observed and the current level is maintained with ≈ 1 nA for more than 10^3 s as shown in Figure 19c. The calculated energy consumption (IVt) is ≈ 400 fJ per spike, which is close to the 1–100 fJ per spike of biological synapses. In 2018, Kumar et al.^[123] also published an article about a transparent 2D perovskite $(\text{C}_4\text{H}_9\text{NH}_3)_2\text{PbBr}_4$ with NiO as the top electrode and ZnO as the bottom electrode as shown in Figure 19d,e. The remarkable property of this device is its transparency. Its average transmittance is more than 70%, and it shows its maximum transmittance of $\approx 75\%$ when the wavelength is 550 nm. This device exhibits $I-V$ sweeps by DC voltages of $0 \rightarrow 2 \rightarrow 0 \rightarrow -2 \rightarrow 0$ V with HRS and LRS. The synaptic behavior of potentiation is also observed by inducing input voltage pulses from 0 to 1.3 V. The current level is gradually increased by increasing the input pulses as

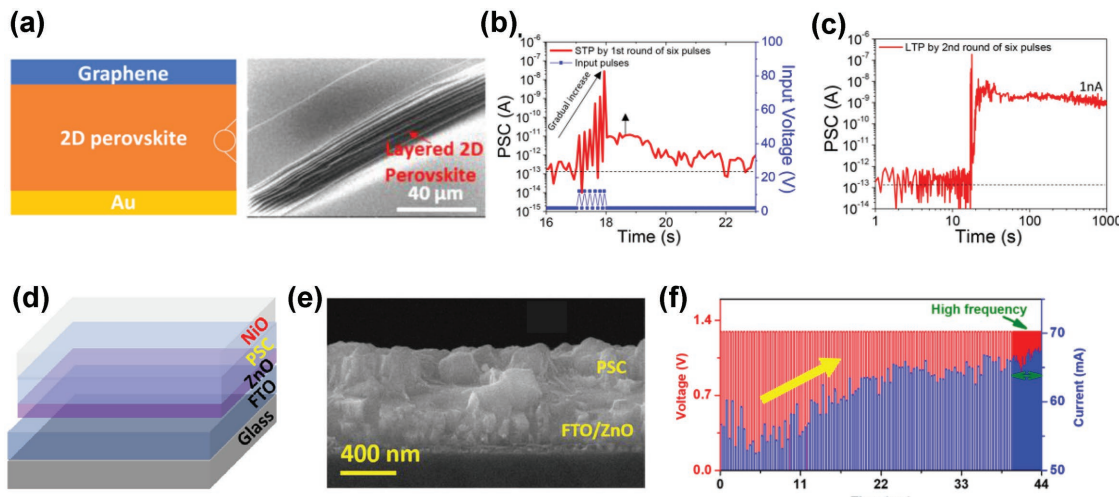


Figure 19. Device structures and synaptic behaviors of artificial synapses which consists of 2D halide perovskites. a) A schematic illustration of graphene/ $(\text{PEA})_2\text{PbBr}_4/\text{Au}$ device, and an SEM image of layered 2D single crystal $(\text{PEA})_2\text{PbBr}_4$. b) An STP behavior by the first set of six pulses. c) An LTP behavior by the second set of six pulses maintaining around 1 nA for the retention of 10^3 s. Reproduced with permission.^[124] Copyright 2017, American Chemical Society. d) A schematic diagram of NiO/PSC/ZnO artificial synapse, where PSC indicates $(\text{C}_4\text{H}_9\text{NH}_3)_2\text{PbBr}_4$. e) Tilted-view SEM image of PSC, the ZnO bottom electrode, and the FTO substrate. f) A synaptic potentiation behavior by DC voltages of $0 \rightarrow 1.3 \rightarrow 0$ V. Reproduced with permission.^[123] Copyright 2018, American Chemical Society.

shown in Figure 19f. From these recent two articles, 2D halide perovskites proved their possibility for artificial synapses, but more functions of synaptic behaviors such as STDP, SRDP, STD, and LTD are required to be examined in the future.

7. Low-Dimensional Materials

7.1. Nanoparticles

Recently, it has been revealed that Ag nanoparticles (NPs) could enhance the performance of resistive switching memories in terms of low power consumption and low switching voltages. Dispersed Ag NPs enhance the Ag filament formation and inhibit the random filament generation and rupture. In 2016, Wang et al.^[47] published an article about $\text{TaN}/\text{Al}_2\text{O}_3/\text{ZnO}/\text{ITO}$ devices with dispersed Ag NPs. The $I-V$ sweeps with HRS and HRS are obtained as memristors, and potentiation and depression behaviors are observed as an artificial synapse.

In particular, polymer–metal NP composites have been researched for memristors and artificial synapses owing to their advantages such as versatile functionality, ductility, low cost, nontoxicity, and biocompatibility. The resistive switching characteristics of organic–metal NPs are related to the properties of the metal and different capping ligands. However, the charge trapping properties of metal NPs are not accurately demonstrated and the ligands could act as unpredictable impurities in the polymer. Hence, the composition of organic–metal NPs should be precisely exhibited in order to generate CF and charge migration for application to memristor-based artificial

synapses. In 2018, Zhou et al.^[48] fabricated an Au–Ag core–shell (Au@Ag) NP composite layer, which works by increasing charge trapping and migration compared to a single-metal component. As shown in Figure 20a, the Au@Ag NPs are perfectly dispersed in the polyvinylpyrrolidone (PVPy) layer and spin-coated on an ITO bottom electrode, and then a gold top electrode is deposited via thermal evaporation through a shadow mask. Through a high-resolution TEM, the size of Au@Ag NPs is determined as ≈ 23 nm, and that of the Au core is observed as 12 nm. The $I-V$ sweeps are successfully investigated with HRS and LRS by applying voltage sweeps of $0 \rightarrow 5 \rightarrow 0 \rightarrow -5 \rightarrow 0$ V to the Ag top electrode. The $I-V$ sweep profiles according to the Au@Ag NP doping concentration are also obtained. The devices show 500 cycles of endurance and a retention time of 10^4 s with an on–off ratio of $\approx 10^3$. It is revealed that the PVPy films work as the charge blocking layer and tunneling material because they have wide band gaps. If a positive voltage is applied on the device, the electrons are increased by SCLC and could be trapped by Au@Ag NPs. When the electrons are fully trapped, the device follows an Ohmic conduction, and the device changes to LRS. When a negative bias is applied on the Ag top electrode, the trapped electrons could be detrapped and migrate to the ITO bottom electrode, changing the device to HRS. The resistive switching of this device is also determined by the formation of the Ag filament. The dispersed Au@Ag NPs work as separate nucleation centers for enhancing the nucleation of Ag atoms, leading to a more effective filament formation. The Ag/PVPy-Au@Ag NPs/ITO device shows synaptic behaviors such as PPF, SRDP, and STDP. According to the pulse interval time, the current increasing rate is varied

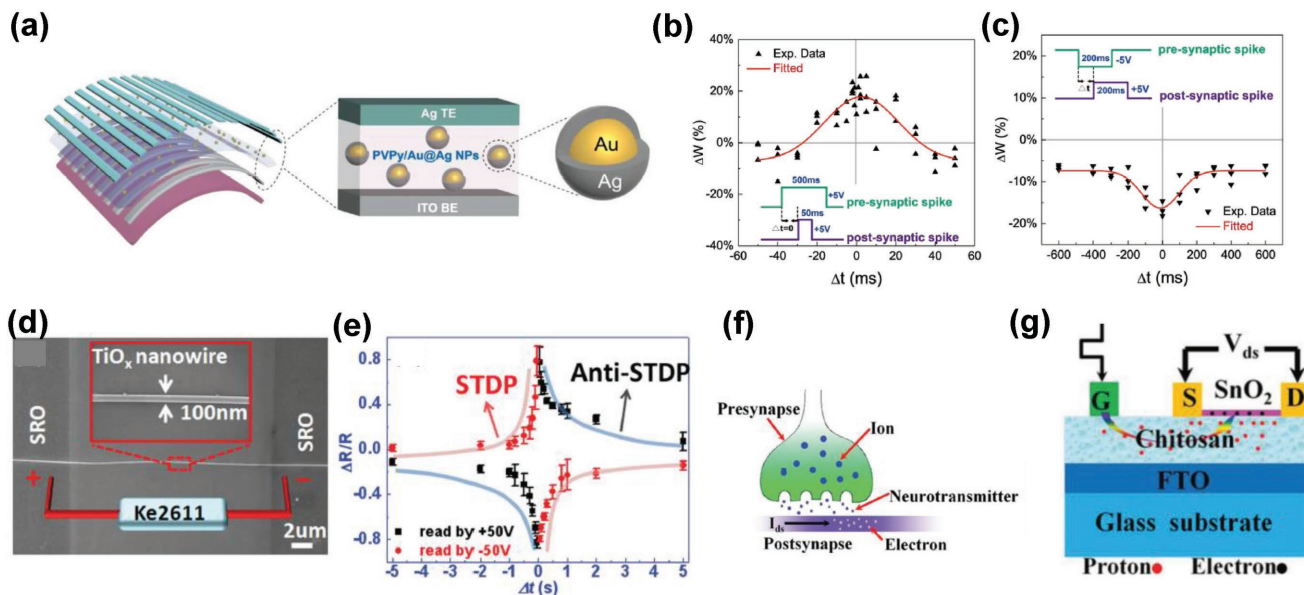


Figure 20. Device structures and synaptic behaviors of electronic synapses based on emerging low-dimensional materials. a) Schematic illustrations of Au@Ag NPs-dispersed PVPy synapse with a Ag top electrode and ITO bottom electrode. b) A STDP behavior which follows symmetric Hebbian learning rule by programmed pre- and postsynaptic spikes. c) A STDP behavior which follows symmetric anti-Hebbian learning rule by another programmed synaptic pre- and postpulses. Reproduced with permission.^[48] Copyright 2018, Wiley-VCH. d) An SEM image of two-terminal synapse with a TiO_x nanowire and SRO electrodes on SrTiO_3 substrate. e) STDP behaviors which follow symmetric Hebbian, and asymmetric anti-Hebbian learning rule by read voltage of ± 50 V. Reproduced with permission.^[49] Copyright 2016, Wiley-VCH. f) A schematic illustration of three-terminal artificial synapse, which emulate neurotransmission in biological synapses. g) A schematic diagram of a synaptic transistor composed of a SnO_2 nanowire channel and chitosan gate. Reproduced with permission.^[50] Copyright 2016, Royal Society of Chemistry.

with the smallest interval of 0.05 s, showing a higher changing rate. As shown in Figure 20b,c, STDP behaviors, which follow the symmetric Hebbian and symmetric anti-Hebbian rules respectively, are observed. By employing Au@Ag NPs as the charge trapping centers and enhancing the Ag filament nucleation region, this device could exhibit resistive switching and synaptic properties.

7.2. Nanowires

Because scaling down has become an important factor for memristive devices, there have been various studies on 1D nanomaterials for resistive switching memories and artificial synapses. In 2016, Hong et al.^[49] reported an article about TiO_x single nanowires, which show synaptic behaviors. As shown in Figure 20d, TiO_2 NWs with a diameter of 100 nm are synthesized by an electrospinning method on the SrTiO_3 substrate with parallel SrRuO_3 (SRO) electrodes. The operating voltage is higher than that of other memristor materials at pulse biases of 80 to 120 V and read pulse biases of ± 50 V. The DC sweep curves are obtained with $0 \rightarrow +200 \rightarrow 0 \rightarrow -200 \rightarrow 0$ V. It is revealed that the redistribution of the oxygen vacancies in the TiO_x NWs determines their diode behavior. By this single-memdiode device, STDP behaviors that follow the asymmetric Hebbian and asymmetric anti-Hebbian learning rules are obtained as shown in Figure 20e. The potentiation and depression behaviors are also discovered through this device.

In 2016, Gou et al.^[50] also published an article about three-terminal artificial synapses with 1D SnO_2 NWs. SnO_2 has excellent advantages of fast ion migration, great stability, and superior optoelectronic properties. They employed a SnO_2 NW as a channel layer as shown in Figure 20f,g. Through this device, the PPF behavior is obtained with a pulse amplitude of 2 V. The SRDP behaviors with different pulse frequencies ranging from 0.33 to 10 Hz are also observed. Ting et al. in 2017^[51] reported on the resistive switching properties of $\text{Ni}@\text{NiO}$ core-shell NWs with a cross structure. The cross structure achieves the possibility of confining the switching region. Through the TEM image, it is discovered that the NiO shell is $\approx 10 \pm 3$ nm and the Ni core has a diameter range of 60 ± 10 nm. The I -V sweep appears as unipolar switching, and a high on-off ratio of 10^7 is obtained. It is found that the working mechanism of forming and SET are based on the oxygen ion migration from the crossbar center to the outside and/or the NiO shell. When the RESET process is implemented, the oxygen ions are transported to the original state from the NiO shell, which leads to a morphological change of the NWs. By controlling the transport of oxygen ions at the cathode, the device could achieve a higher scale-down ability and show the possibility of being applied to electronic synapses.

8. Summary and Prospective

Overall, memristors have the advantages of scalability, less energy consumption, and ultrafast data processing speed, which satisfy the requirements of neuromorphic computing. Various memristors achieve not only reliable memory properties but also excellent synaptic behaviors.

Metal oxides are the most popular memristive materials. Because they have been researched for a long time, many papers showing their remarkable synaptic properties have been published. Recently, researchers are focused on the device structure instead of the materials themselves. By manipulating the device structure, the working mechanism is changed, and the switching behaviors are also affected with their speed and shape. In particular, through heterojunction structures composed of ion-rich layer and ion-diffusion limiting layer, the speed of device conductance could be easily controlled. Hence, synaptic behaviors accompanied with gradual current changes could be achieved. Amorphous oxide semiconductors and perovskite oxides are considered as new oxide materials for artificial synapses. One of the amorphous oxides, IGZO could be formed as a noticeable ion-rich layer. Hence, a heterojunction and/or three-terminal structure is applied for controlling the ion tunneling at the interface between IGZO and a top electrode. Similarly, perovskite oxides have advantages of localized accumulation of oxygen ions; thus, the switching mechanism is generally the interface type. Different from BFO, which has been reported as a two-terminal structure, SNO is utilized for three-terminal synaptic transistors and it achieves STDP, potentiation, and depression behaviors. In contrast to two-terminal devices, three-terminal synapses could implement stimuli transmission and learning process at the same time.

Different from inorganic memristors, polymer memristors are biocompatible, low cost, and nontoxic. Polymers could be fabricated by simple solution processes. A remarkable advantage of polymer memristors is that they could easily modulate the electrical performance by a designed molecular synthesis. They change their conductance by changing their intrinsic properties through redox reaction, phase and conformation change, and charge transferring. Including PEDOT:PSS, there have been many advancements in polymer-based synapses that achieve synaptic behaviors such as STDP, SRDP, potentiation, and depression. As organic materials, bioinspired organics have also been employed for memristors and artificial synapses. They have similar advantages to polymer memristors such as biocompatibility, nontoxicity, and low cost. Recently, lignin extracted from woods, chitosan, protein from chicken albumen, and *t*-car seaweed with excellent synaptic behaviors of STDP, SRDP, EPSC, LTP, and LTD have been reported.

Furthermore, 2D materials such as graphene and MoS_2 have been actively researched recently for synaptic behaviors owing to their remarkable advantages. Graphene is composed of a 2D array of carbon, which appears with a honeycomb lattice. It has excellent advantages such as flexibility, low cost, non-toxicity, and biocompatibility. Graphene could be utilized as a flexible bottom electrode or dielectric material. Both monolayer and multilayer graphenes have been employed for two-terminal or three-terminal structures as a dielectric material and have shown successful synaptic behaviors such as SRDP and LTM. It is revealed that the multilayer graphene could utilize its nanopores for inhibiting a rapid resistance change by blocking the ion transport. Each layer could suppress the other layers' nanopores and block the ion transport path. GQDs also achieve memory properties and synaptic behaviors such as STDP and SRDP. As a promising 2D material, MoS_2 has been considered as substitute to graphene. Different from graphene with a

zero band gap, MoS₂ has a band gap between 1.2 eV of bulk to 1.8 eV of monolayers. MoS₂ is employed as a dielectric layer in two-terminal or three-terminal synaptic transistors. Through an oxidation process, it generates ion vacancies and results in synaptic behaviors with device conductance changes. It is reported that GBs in MoS₂ could be easily modulated for the control of resistance changes.

In recent years, halide perovskites have been highlighted owing to their rapid ion migration, solution process possibility, tunable band gap, and long charge-carrier diffusion length. Using electrochemically active electrodes such as Ag and Cu, halide perovskite-based memristors show ultralow operating voltages, high on-off ratios (>10⁹), and rapid operation time. Hence, it has drawn attention from researchers in the memory field. Most recently, in 2016, it has been reported that halide perovskite memristors successfully achieve synaptic behaviors of potentiation, depression, LTP, STP, SRDP, and STDP.

Low-dimensional materials such as Ag NPs and nanowires have also been actively reported recently as promising candidates for artificial synapses. Dispersed Ag NPs could act as Ag nucleation center during the Ag filament formation process. Hence, they enhance the Ag filament formation and inhibit the random filament generation and rupture. Synaptic properties such as PPF, SRDP, and STDP are observed from memristors with Ag NPs. Nanowires have excellent scalability and show synaptic behaviors such as STDP and SRDP.

Even though considerable advances have been attained as mentioned above, memristor-based artificial synapses need to be improved for real-life applications. Memristive synapses have achieved only several parts of brain functions. Complementary to the recent developments, there are many brain functions such as cognitive, sensory, and linguistic operations that are required. Therefore, advanced structures with suitable programmed voltages and new materials should be developed. Second, memristors have weak points of uncontrollable CF and unavoidable electroforming processes, which make it complicated to use them for large-scale system integration. Thus, further studies for controlling resistive switching profiles are strongly required. Lastly, to complement the current advances, the deficiencies of each memristive material should be overcome. Oxide memristors have excellent endurance characteristics but have small on-off ratios. 2D and emerging materials can only meet several synaptic behaviors. They need to achieve more brain functions through suitable structure designs, pulse voltage programming, and improving synthesis methods for real-life applications. Halide perovskites have been causing problems with their unstable structures, hindering their large-scale applications. Therefore, continuous studies should be conducted to find solutions to weak points of each material. We believe that neuromorphic architecture composed of artificial synapses could substitute the current CMOS technology in the near future through continuous advances in memristive materials.

Acknowledgements

This work was financially supported by the Future Material Discovery Program (2016M3D1A1027666) and the Basic Science Research Program (2017R1A2B3009135) through the National Research Foundation of Korea. This article is part of the special series on *Advanced Intelligent*

Systems that showcases the outstanding achievements of leading international researchers on intelligent systems.

Conflict of Interest

The authors declare no conflict of interest.

Keywords

artificial synapses, memories, memristors, memtransistors, neuromorphic architectures

Received: September 20, 2018

Revised: October 7, 2018

Published online: November 8, 2018

-
- [1] L. Chua, *IEEE Trans. Circuit Theory* **1971**, *18*, 507.
 - [2] H. Kim, J. S. Han, J. Choi, S. Y. Kim, H. W. Jang, *Small Methods* **2018**, *2*, 1700310.
 - [3] J. Choi, J. S. Han, K. Hong, S. Y. Kim, H. W. Jang, *Adv. Mater.* **2018**, *30*, 1704002.
 - [4] Z. Y. Wang, L. Y. Wang, M. Nagai, L. H. Xie, M. D. Yi, W. Huang, *Adv. Electron. Mater.* **2017**, *3*, 1600510.
 - [5] W. Xu, H. Cho, Y. H. Kim, Y. T. Kim, C. Wolf, C. G. Park, T. W. Lee, *Adv. Mater.* **2016**, *28*, 5916.
 - [6] D. Kuzum, S. M. Yu, H. S. P. Wong, *Nanotechnology* **2013**, *24*, 382001.
 - [7] D. Sarkar, J. Tao, W. Wang, Q. F. Lin, M. Yeung, C. H. Ren, R. Kapadia, *ACS Nano* **2018**, *12*, 1656.
 - [8] G. Indiveri, E. Chicca, R. Douglas, *IEEE Trans. Neural Networks* **2006**, *17*, 211.
 - [9] R. H. Hahnloser, R. Sarpeshkar, M. A. Mahowald, R. J. Douglas, H. S. Seung, *Nature* **2000**, *405*, 947.
 - [10] C. Diorio, P. Hasler, A. Minch, C. A. Mead, *IEEE Trans. Electron Devices* **1996**, *43*, 1972.
 - [11] L. Chen, Z. Y. He, T. Y. Wang, Y. W. Dai, H. Zhu, Q. Q. Sun, D. W. Zhang, *Electronics* **2018**, *7*, 80.
 - [12] S. Brivio, E. Covi, A. Serb, T. Prodromakis, M. Fanciulli, S. Spiga, *Appl. Phys. Lett.* **2016**, *109*, 133504.
 - [13] K. V. Egorov, R. V. Kirtaev, Y. Y. Lebedinskii, A. M. Markeev, Y. A. Matveyev, O. M. Orlov, A. V. Zablotskiy, A. V. Zenkevich, *Phys. Status Solidi A* **2015**, *212*, 809.
 - [14] G. Niu, P. Calka, M. A. der Maur, F. Santoni, S. Guha, M. Fraschke, P. Hamoumou, B. Gautier, E. Perez, C. Walczyk, C. Wenger, A. Di Carlo, L. Alff, T. Schroeder, *Sci. Rep.* **2016**, *6*, 25757.
 - [15] A. Padovani, J. Woo, H. Hwang, L. Larcher, *IEEE Electron Device Lett.* **2018**, *39*, 672.
 - [16] a) J. Woo, K. Moon, J. Song, S. Lee, M. Kwak, J. Park, H. Hwang, *IEEE Electron Device Lett.* **2016**, *37*, 994; b) J. Woo, D. Lee, Y. Koo, H. Hwang, *Microelectron. Eng.* **2017**, *182*, 42.
 - [17] Z. W. Wang, M. H. Yin, T. Zhang, Y. M. Cai, Y. Y. Wang, Y. C. Yang, R. Huang, *Nanoscale* **2016**, *8*, 14015.
 - [18] X. J. Zhu, C. Du, Y. Jeong, W. D. Lu, *Nanoscale* **2017**, *9*, 45.
 - [19] C. Du, W. Ma, T. Chang, P. Sheridan, W. D. Lu, *Adv. Funct. Mater.* **2015**, *25*, 4290.
 - [20] L. Tao, Z. Kailiang, W. Fang, S. Kuo, S. Wenxiang, Z. Jinshi, *ECS Trans.* **2013**, *52*, 1003.
 - [21] Z. H. Tan, R. Yang, K. Terabe, X. B. Yin, X. D. Zhang, X. Guo, *Adv. Mater.* **2016**, *28*, 377.
 - [22] J. Shi, S. D. Ha, Y. Zhou, F. Schoofs, S. Ramanathan, *Nat. Commun.* **2013**, *4*, 2676.

- [23] N. Du, M. Kiani, C. G. Mayr, T. G. You, D. Burger, I. Skorupa, O. G. Schmidt, H. Schmidt, *Front. Neurosci.* **2015**, *9*, 227.
- [24] C. Mayr, P. Staerke, J. Partzsch, L. Cederstroem, R. Schüffny, Y. Shuai, N. Du, H. Schmidt, *5th Int. Conf. Neural Inf. Proc. Syst.* **2012**, *1*, 1700.
- [25] L. Cederström, P. Stärke, C. Mayr, Y. Shuai, H. Schmid, R. Schüffny, presented at 2013 IEEE Int. Symp. on Circuits and Systems (ISCAS2013), Beijing, China, May **2013**.
- [26] Y. van de Burgt, E. Lubberman, E. J. Fuller, S. T. Keene, G. C. Faria, S. Agarwal, M. J. Marinella, A. A. Talin, A. Salleo, *Nat. Mater.* **2017**, *16*, 414.
- [27] A. Bandyopadhyay, S. Sahu, M. Higuchi, *J. Am. Chem. Soc.* **2011**, *133*, 1168.
- [28] S. Z. Li, F. Zeng, C. Chen, H. Y. Liu, G. S. Tang, S. Gao, C. Song, Y. S. Lin, F. Pan, D. Guo, *J. Mater. Chem. C* **2013**, *1*, 5292.
- [29] C. Wu, T. W. Kim, H. Y. Choi, D. B. Strukov, J. J. Yang, *Nat. Commun.* **2017**, *8*, 752.
- [30] G. Liu, C. Wang, W. B. Zhang, L. Pan, C. C. Zhang, X. Yang, F. Fan, Y. Chen, R. W. Li, *Adv. Electron. Mater.* **2016**, *2*, 1500298.
- [31] Y. Park, J. S. Lee, *ACS Nano* **2017**, *11*, 8962.
- [32] Y. H. Liu, L. Q. Zhu, P. Feng, Y. Shi, Q. Wan, *Adv. Mater.* **2015**, *27*, 5599.
- [33] N. R. Hosseini, J. S. Lee, *Adv. Funct. Mater.* **2015**, *25*, 5586.
- [34] N. R. Hosseini, J. S. Lee, *ACS Appl. Mater. Interfaces* **2016**, *8*, 7326.
- [35] H. Wang, F. B. Meng, B. W. Zhu, W. R. Leow, Y. Q. Liu, X. D. Chen, *Adv. Mater.* **2015**, *27*, 7670.
- [36] G. D. Wu, P. Feng, X. Wan, L. Q. Zhu, Y. Shi, Q. Wan, *Sci. Rep.* **2016**, *6*, 23578.
- [37] K. S. Novoselov, A. K. Geim, S. V. Morozov, D. Jiang, Y. Zhang, S. V. Dubonos, I. V. Grigorieva, A. A. Firsov, *Science* **2004**, *306*, 666.
- [38] Y. Zhu, S. Murali, W. Cai, X. Li, J. W. Suk, J. R. Potts, R. S. Ruoff, *Adv. Mater.* **2010**, *22*, 3906.
- [39] Z. S. Siwy, M. Davenport, *Nat. Nanotechnol.* **2010**, *5*, 697.
- [40] H. Tian, W. T. Mi, H. M. Zhao, M. A. Mohammad, Y. Yang, P. W. Chiu, T. L. Ren, *Nanoscale* **2017**, *9*, 9275.
- [41] J. Lee, C. Du, K. Sun, E. Kioupakis, W. D. Lu, *ACS Nano* **2016**, *10*, 3571.
- [42] J. Jiang, J. J. Guo, X. Wan, Y. Yang, H. P. Xie, D. M. Niu, J. L. Yang, J. He, Y. L. Gao, Q. Wan, *Small* **2017**, *13*, 1700933.
- [43] A. A. Bessonov, M. N. Kirikova, D. I. Petukhov, M. Allen, T. Ryhanen, M. J. A. Bailey, *Nat. Mater.* **2015**, *14*, 199.
- [44] V. K. Sangwan, D. Jariwala, I. S. Kim, K.-S. Chen, T. J. Marks, L. J. Lauhon, M. C. Hersam, *Nat. Nanotechnol.* **2015**, *10*, 403.
- [45] Z. G. Xiao, J. S. Huang, *Adv. Electron. Mater.* **2016**, *2*, 1600100.
- [46] E. Yoo, M. Lyu, J. H. Yun, C. Kang, Y. Choi, L. Z. Wang, *J. Mater. Chem. C* **2016**, *4*, 7824.
- [47] D. T. Wang, Y. W. Dai, J. Xu, L. Chen, Q. Q. Sun, P. Zhou, P. F. Wang, S. J. Ding, D. W. Zhang, *IEEE Electron Device Lett.* **2016**, *37*, 878.
- [48] L. Zhou, J. Y. Mao, Y. Ren, J. Q. Yang, S. R. Zhang, Y. Zhou, Q. F. Liao, Y. J. Zeng, H. Q. Shan, Z. X. Xu, J. J. Fu, Y. Wang, X. L. Chen, Z. Y. Lv, S. T. Han, V. A. L. Roy, *Small* **2018**, *14*, 1800288.
- [49] D. S. Hong, Y. S. Chen, J. R. Sun, B. G. Shen, *Adv. Electron. Mater.* **2016**, *2*, 1500359.
- [50] G. Y. Gou, J. Sun, C. Qian, Y. K. He, L. A. Kong, Y. Fu, G. Z. Dai, J. L. Yang, Y. L. Gao, *J. Mater. Chem. C* **2016**, *4*, 11110.
- [51] Y. H. Ting, J. Y. Chen, C. W. Huang, T. K. Huang, C. Y. Hsieh, W. W. Wu, *Small* **2018**, *14*, 1703153.
- [52] R. Waser, *Nanoelectronics and Information Technology: Advanced Electronic Materials and Novel Devices*, Wiley-VCH, Weinheim, Germany **2012**.
- [53] R. Waser, R. Dittmann, G. Staikov, K. Szot, *Adv. Mater.* **2009**, *21*, 2632.
- [54] Y. C. Yang, P. Gao, S. Gaba, T. Chang, X. Q. Pan, W. Lu, *Nat. Commun.* **2012**, *3*, 1737.
- [55] Y. C. Yang, P. Gao, L. Z. Li, X. Q. Pan, S. Tappertzhofen, S. Choi, R. Waser, I. Valov, W. D. Lu, *Nat. Commun.* **2014**, *5*, 5232.
- [56] A. Sawa, *Mater. Today* **2008**, *11*, 28.
- [57] S. Bagdzevicius, K. Maas, M. Boudard, M. Burriel, *J. Electroceram.* **2017**, *39*, 157.
- [58] Hadiyawarmann, F. Budiman, D. G. O. Hernowo, R. R. Pandey, H. Tanaka, *Jpn. J. Appl. Phys.* **2018**, *57*, 03EA06.
- [59] B. Qu, A. Younis, D. W. Chu, *Electron. Mater. Lett.* **2016**, *12*, 715.
- [60] B. Gao, J. F. Kang, Z. Zhou, Z. Chen, P. Huang, L. F. Liu, X. Y. Liu, *Jpn. J. Appl. Phys.* **2016**, *55*, 04EA06.
- [61] V. M. Ho, J. A. Lee, K. C. Martin, *Science* **2011**, *334*, 623.
- [62] L. F. Abbott, S. B. Nelson, *Nat. Neurosci.* **2000**, *3*, 1178.
- [63] M. Ziegler, C. Riggert, M. Hansen, T. Bartsch, H. Kohlstedt, *IEEE Trans. Biomed. Circuits Syst.* **2015**, *9*, 197.
- [64] N. Caporale, Y. Dan, *Annu. Rev. Neurosci.* **2008**, *31*, 25.
- [65] Y. Li, Y. P. Zhong, J. J. Zhang, L. Xu, Q. Wang, H. J. Sun, H. Tong, X. M. Cheng, X. S. Miao, *Sci. Rep.* **2015**, *4*, 4906.
- [66] G. Q. Bi, M. M. Poo, *J. Neurosci.* **1998**, *18*, 10464.
- [67] T. Ohno, T. Hasegawa, T. Tsuruoka, K. Terabe, J. K. Gimzewski, M. Aono, *Nat. Mater.* **2011**, *10*, 591.
- [68] G. Rachmuth, H. Z. Shouval, M. F. Bear, C. S. Poon, *Proc. Natl. Acad. Sci. USA* **2011**, *108*, E1266.
- [69] R. C. Malenka, *Cell* **1994**, *78*, 535.
- [70] R. C. Atkinson, R. M. Shiffrin, *Psychology of Learning and Motivation*, Vol. 2, Elsevier, Standford, CA **1968**, p. 89.
- [71] R. Berdan, E. Vasilaki, A. Khiat, G. Indiveri, A. Serb, T. Prodromakis, *Sci. Rep.* **2016**, *6*, 18639.
- [72] X. Zhu, C. Du, Y. Jeong, W. D. Lu, *Nanoscale* **2017**, *9*, 45.
- [73] Y. Yang, M. Yin, Z. Yu, Z. Wang, T. Zhang, Y. Cai, W. D. Lu, R. Huang, *Adv. Electron. Mater.* **2017**, *3*, 1700032.
- [74] J. J. Yang, F. Miao, M. D. Pickett, D. A. A. Ohlberg, D. R. Stewart, C. N. Lau, R. S. Williams, *Nanotechnology* **2009**, *20*, 215201.
- [75] J. H. Yoon, Z. R. Wang, K. M. Kim, H. Q. Wu, V. Ravichandran, Q. F. Xia, C. S. Hwang, J. J. Yang, *Nat. Commun.* **2018**, *9*, 417.
- [76] J. S. Han, Q. V. Le, J. Choi, K. Hong, C. W. Moon, T. L. Kim, H. Kim, S. Y. Kim, H. W. Jang, *Adv. Funct. Mater.* **2018**, *28*, 1705783.
- [77] J. Choi, S. Park, J. Lee, K. Hong, D. H. Kim, C. W. Moon, G. D. Park, J. Suh, J. Hwang, S. Y. Kim, H. S. Jung, N. G. Park, S. Han, K. T. Nam, H. W. Jang, *Adv. Mater.* **2016**, *28*, 6562.
- [78] M. K. Kim, J. S. Lee, *ACS Nano* **2018**, *12*, 1680.
- [79] Y. Hirose, H. Hirose, *J. Appl. Phys.* **1976**, *47*, 2767.
- [80] D. S. Jeong, C. S. Hwang, *Adv. Mater.* **2018**, *30*, 1704729.
- [81] F. Pan, S. Gao, C. Chen, C. Song, F. Zeng, *Mater. Sci. Eng., R* **2014**, *83*, 1.
- [82] S. Gao, C. Song, C. Chen, F. Zeng, F. Pan, *Appl. Phys. Lett.* **2013**, *102*, 141606.
- [83] Y. Sun, M. Tai, C. Song, Z. Wang, J. Yin, F. Li, H. Wu, F. Zeng, H. Lin, F. Pan, *J. Phys. Chem. C* **2018**, *122*, 6431.
- [84] D. Garbin, E. Vianello, O. Bichler, Q. Rafhay, C. Gamrat, G. Ghibaudo, B. DeSalvo, L. Perniola, *IEEE Trans. Electron Devices* **2015**, *62*, 2494.
- [85] C. Chen, C. Song, J. Yang, F. Zeng, F. Pan, *Appl. Phys. Lett.* **2012**, *100*, 253509.
- [86] P. B. Pillai, M. M. De Souza, *ACS Appl. Mater. Interfaces* **2017**, *9*, 1609.
- [87] T. Shi, R. Yang, X. Guo, *Solid State Ionics* **2016**, *296*, 114.
- [88] H. Nili, S. Walia, A. E. Kandjani, R. Ramanathan, P. Gutruf, T. Ahmed, S. Balendhran, V. Bansal, D. B. Strukov, O. Kavehei, M. Bhaskaran, S. Sriram, *Adv. Funct. Mater.* **2015**, *25*, 3172.
- [89] D.-H. Kwon, K. M. Kim, J. H. Jang, J. M. Jeon, M. H. Lee, G. H. Kim, X.-S. Li, G.-S. Park, B. Lee, S. Han, *Nat. Nanotechnol.* **2010**, *5*, 148.
- [90] B. Hwang, J. S. Lee, *Nanoscale* **2018**, *10*, 8578.
- [91] M. Hansen, M. Ziegler, L. Kolberg, R. Soni, S. Dirkmann, T. Mussenbrock, H. Kohlstedt, *Sci. Rep.* **2015**, *5*, 13753.

- [92] T. Dongale, N. Mullani, V. Patil, R. Tikke, P. Pawar, S. Mohite, A. Teli, A. Bagade, K. Pawar, K. Khot, *J. Nanosci. Nanotechnol.* **2018**, *18*, 7758.
- [93] R. B. Pan, J. Li, F. Zhuge, L. Q. Zhu, L. Y. Liang, H. L. Zhang, J. H. Gao, H. T. Cao, B. Fu, K. Li, *Appl. Phys. Lett.* **2016**, *108*, 013504.
- [94] S. M. Yu, Y. Wu, R. Jeyasingh, D. G. Kuzum, H. S. P. Wong, *IEEE Trans. Electron Devices* **2011**, *58*, 2729.
- [95] C. H. Wang, W. He, Y. Tong, R. Zhao, *Sci. Rep.* **2016**, *6*, 22970.
- [96] Z. Wang, S. Joshi, S. E. Savel'ev, H. Jiang, R. Midya, P. Lin, M. Hu, N. Ge, J. P. Strachan, Z. Li, *Nat. Mater.* **2017**, *16*, 101.
- [97] S. Kim, C. Du, P. Sheridan, W. Ma, S. Choi, W. D. Lu, *Nano Lett.* **2015**, *15*, 2203.
- [98] Z. Q. Wang, H. Y. Xu, X. H. Li, H. Yu, Y. C. Liu, X. J. Zhu, *Adv. Funct. Mater.* **2012**, *22*, 2759.
- [99] J. M. Zhou, N. Liu, L. Q. Zhu, Y. Shi, Q. Wan, *IEEE Electron Device Lett.* **2015**, *36*, 198.
- [100] L. Q. Zhu, C. J. Wan, L. Q. Guo, Y. Shi, Q. Wan, *Nat. Commun.* **2014**, *5*, 3158.
- [101] X. Wan, Y. Yang, P. Feng, Y. Shi, Q. Wan, *IEEE Electron Device Lett.* **2016**, *37*, 299.
- [102] C. J. Wan, Y. H. Liu, L. Q. Zhu, P. Peng, Y. Shi, Q. Wan, *ACS Appl. Mater. Interfaces* **2016**, *8*, 9762.
- [103] R. Jiang, P. F. Ma, Z. Y. Han, X. H. Du, *Sci. Rep.* **2017**, *7*, 9354.
- [104] M. Moors, K. K. Adepalu, Q. Y. Lu, A. Wedig, C. Baumer, K. Skaja, B. Arndt, H. L. Tuller, R. Dittmann, R. Waser, B. Yildiz, I. Valov, *ACS Nano* **2016**, *10*, 1481.
- [105] Y. Chen, G. Liu, C. Wang, W. B. Zhang, R. W. Li, L. X. Wang, *Mater. Horiz.* **2014**, *1*, 489.
- [106] K. Kostarelos, K. S. Novoselov, *Nat. Nanotechnol.* **2014**, *9*, 744.
- [107] H. Tian, W. T. Mi, X. F. Wang, H. M. Zhao, Q. Y. Xie, C. Li, Y. X. Li, Y. Yang, T. L. Ren, *Nano Lett.* **2015**, *15*, 8013.
- [108] Y.-C. Chen, S.-T. Hu, C.-Y. Lin, B. Fowler, H.-C. Huang, C.-C. Lin, S. Kim, Y.-F. Chang, J. C. Lee, *Nanoscale* **2018**, *10*, 15608.
- [109] C. J. Wan, L. Q. Zhu, Y. H. Liu, P. Feng, Z. P. Liu, H. L. Cao, P. Xiao, Y. Shi, Q. Wan, *Adv. Mater.* **2016**, *28*, 3557.
- [110] Y. Yang, J. Wen, L. Q. Guo, X. Wan, P. F. Du, P. Feng, Y. Shi, Q. Wan, *ACS Appl. Mater. Interfaces* **2016**, *8*, 30281.
- [111] J. S. Bunch, S. S. Verbridge, J. S. Alden, A. M. Van Der Zande, J. M. Parpia, H. G. Craighead, P. L. McEuen, *Nano Lett.* **2008**, *8*, 2458.
- [112] S. Garaj, W. Hubbard, A. Reina, J. Kong, D. Branton, J. Golovchenko, *Nature* **2010**, *467*, 190.
- [113] S. C. O'Hern, C. A. Stewart, M. S. Boutilier, J.-C. Idrobo, S. Bhaviripudi, S. K. Das, J. Kong, T. Laoui, M. Atieh, R. Karnik, *ACS Nano* **2012**, *6*, 10130.
- [114] H. Y. Choi, C. Wu, C. H. Bok, T. W. Kim, *NPG Asia Mater.* **2017**, *9*, e413.
- [115] A. J. Arnold, A. Razavieh, J. R. Nasr, D. S. Schulman, C. M. Eichfeld, S. Das, *ACS Nano* **2017**, *11*, 3110.
- [116] V. K. Sangwan, H. S. Lee, H. Bergeron, I. Balla, M. E. Beck, K. S. Chen, M. C. Hersam, *Nature* **2018**, *554*, 500.
- [117] Y. Yuan, J. Huang, *Acc. Chem. Res.* **2016**, *49*, 286.
- [118] J. Choi, Q. V. Le, K. Hong, C. W. Moon, J. S. Han, K. C. Kwon, P. R. Cha, Y. Kwon, S. Y. Kim, H. W. Jang, *ACS Appl. Mater. Interfaces* **2017**, *9*, 30764.
- [119] A. Walsh, *J. Phys. Chem. C* **2015**, *119*, 5755.
- [120] G. Xing, N. Mathews, S. Sun, S. S. Lim, Y. M. Lam, M. Grätzel, S. Mhaisalkar, T. C. Sum, *Science* **2013**, *342*, 344.
- [121] B. Hwang, J. S. Lee, *Adv. Mater.* **2017**, *29*, 1701048.
- [122] C. Eames, J. M. Frost, P. R. F. Barnes, B. C. O'Regan, A. Walsh, M. S. Islam, *Nat. Commun.* **2015**, *6*, 7497.
- [123] M. Kumar, H. S. Kim, D. Y. Park, M. S. Jeong, J. Kim, *ACS Appl. Mater. Interfaces* **2018**, *10*, 12768.
- [124] H. Tian, L. F. Zhao, X. F. Wang, Y. W. Yeh, N. Yao, B. P. Rand, T. L. Ren, *ACS Nano* **2017**, *11*, 12247.
- [125] B. Zhang, G. Liu, Y. Chen, C. Wang, K. G. Neoh, T. Bai, E. T. Kang, *ChemPlusChem* **2012**, *77*, 74.